Evaluating trace-metal responses to field deployment of enhanced rock weathering across agricultural and riparian soils

Quinn C. Zacharias[1,2*], Robert Rioux[1,2], Fengchao Sun[1,2], Wyatt Tatge[1,2], Joshua L. Warren[3], Peter A. Raymond[1,2], James E. Saiers[1,2]

[1]Yale University, School of the Environment, New Haven, United States

[2]Yale Center for Natural Carbon Capture, New Haven, United States

[3]Yale University, Department of Biostatistics, New Haven, United States

*Corresponding author: Quinn C. Zacharias, quinn.zacharias@yale.edu

Keywords: Enhanced rock weathering, risk assessment, soil metal stabilization, basalt amendment

Abstract

Enhanced rock weathering (ERW) is proposed for carbon dioxide removal, but responsible field deployment requires careful evaluation of potential trace-metal risks. We applied finely crushed, Fe–Al-rich basalt (20 t ha^{-1}) to the soil surface of hayfield and pasture soils in a working Vermont dairy agroecosystem and monitored an adjacent riparian corridor hydrologically connected to the treated fields. Agricultural surface soils (0–15 cm) were sampled twice before application (fall 2022 and spring 2023) and four times afterward (fall 2023; spring 2024; fall 2024; spring 2025), and riparian soils were sampled once before application and during four post-treatment campaigns. Forage biomass and tissue chemistry were measured at first cut in spring 2023 (pre-treatment) and spring 2024 (one year post-treatment). Extractable soil metals were quantified using the Modified Morgan extractant. In agricultural plots, extractable Ni, Cr, Pb, Al, Mn, Zn, Cu, and Cd did not increase relative to controls, and forage yields and tissue metal concentrations did not differ between treatments. Across plots, extractable Ni, Al, and Pb covaried most strongly with soil pH. Downslope riparian soils exhibited large declines (60–80%) in extractable Ni, Al, and Pb, coincident with a transient rise in extractable Ca:Al ratios. These coupled soil and groundwater patterns are consistent with reduced metal lability in hydrologically connected riparian soils where basalt-derived solutes accumulated. Together, these results indicate that agronomic-rate applications of Fe–Al-rich basalt pose minimal trace-metal risk in treated fields and promote conditions consistent with trace-metal sequestration in zones of weathering product accumulation. Effective ERW monitoring should consider hydrologic connectivity and track soil pH and Ca:Al ratios as practical indicators of evolving metal availability.

Introduction

Terrestrial enhanced rock weathering (ERW) is gaining attention as a negative-emissions pathway for carbon dioxide removal (CDR) (Beerling et al., 2025). In ERW, finely crushed silicate rocks, most often basalt, are applied to soils to accelerate dissolution, supplying alkalinity and base cations that draw down atmospheric CO_2 and can also improve soil fertility (Chiaravalloti et al., 2023; Johnson et al., 2025; Zhang et al., 2023). As Ca- and Mg-bearing silicates dissolve, they consume protons and convert dissolved CO_2 to bicarbonate, generating alkalinity that can be exported as dissolved inorganic carbon to downstream waters and the ocean, where storage occurs on timescales of 10^3–10^5 years (Beerling et al., 2020). Finely crushed basalt suitable for ERW is produced in large volumes through quarrying and aggregate industries and is widely available, making it a scalable ERW feedstock (Power et al., 2023). Environmental stewardship, however, requires understanding how accelerated weathering influences trace metals that may enter soil–plant–water pathways (Bell et al., 2024; Flipkens et al., 2021; Zhang et al., 2024). Although risk discussions often emphasize nickel (Ni) and chromium (Cr) because they are characteristic of mafic and ultramafic materials (Haque et al., 2020), ERW can also alter the lability of other agronomically and toxicologically relevant elements (e.g., Mn, Cu, Zn, Pb, Al) depending on feedstock mineralogy and soil chemistry (Jamieson et al., 2025).

In the context of ERW, assessing exposure risk of trace metals in soils is governed by soil-chemical controls on metal lability, specifically the speciation, mobility, and accessibility of metals in soil solution and exchangeable pools, rather than by total concentrations per se (Gupta et al., 1996; Olaniran et al., 2013). In agronomic systems, plant growth responses largely reflect

this balance at the root zone, where elevated metal lability can impair nutrient acquisition (Kochian et al., 2015; Marschner, 2011), although under strongly acidic or high-exposure conditions, metals may also translocate into plant tissues (Clemens et al., 2013; Nagajyoti et al., 2010). ERW perturbs this balance between metal lability and total concentrations by introducing reactive mineral surfaces and weathering products. Initial dissolution can release structurally bound metals, but these reactions also raise soil pH and promote sorption and secondary-phase formation (e.g., Fe/Al (hydr)oxides), thereby stabilizing cationic metals and shrinking extractable pools (Cornell & Schwertmann, 2003; Ni et al., 2009). Net mobilization versus immobilization, therefore, reflects a competition between transient release and longer-term scavenging as soils evolve toward a new steady state.

Field evidence indicates that ERW outcomes depend strongly on feedstock mineralogy, soil buffering capacity, and dissolution kinetics (Deng et al., 2023; Vandeginste et al., 2024). Multi-year trials with Fe–Al-rich basalts generally report rising pH and no increase in labile Ni or Cr at agronomic application rates (Beerling et al., 2024; Dupla et al., 2024; Kelland et al., 2020). In contrast, olivine-rich and ultramafic materials have increased Ni mobility because they contain higher intrinsic Ni loads and supply less reactive Fe–Al for secondary-oxide formation (Flipkens et al., 2021; Ten Berge et al., 2012; Vienne et al., 2022). These contrasts demonstrate that accelerated weathering can mobilize or immobilize trace metals depending on mineralogical composition and site conditions. However, most existing ERW studies focus on plot-scale soil responses and do not evaluate how weathering-derived solutes influence trace-metal lability in hydrologically connected downslope environments. Field-scale assessments that integrate agricultural soils, vegetation uptake, and receiving riparian zones remain limited.

ERW generates alkalinity and base cations that are mobilized along surface and shallow subsurface flow paths, allowing its geochemical effects to extend beyond amended plots (Pohlmann et al., 2016). Elevated alkalinity and base-cation concentrations in drainage waters following ERW deployments show that silicate-derived solutes can be transported downslope and downstream, yet the roles of near-stream soils, riparian zones, ditches, and other reactive interfaces in storing, transforming, or transmitting these solutes, and associated trace metals, remain poorly constrained (Naiman & DeCamps, 1997; Shao et al., 2015; Sun et al., 2025). This matters even on relatively flat fields: exported solutes may still interact with hydrologically downgradient reactive interfaces before reaching surface waters (Ledesma et al., 2013). Riparian soils are often organic-rich and hydrologically dynamic, and they can buffer geochemical perturbations by exchanging and retaining base cations, altering pH, and providing reactive surfaces that modulate metal lability (Naiman & DeCamps, 1997). In forested and riparian soils, the molar ratio of calcium to aluminum (hereafter, Ca:Al ratio) is widely used as an integrative indicator of metal stress, reflecting competition between Ca^{2+} and exchangeable Al^{3+} (Gu et al., 2017). Quantifying whether ERW-derived solutes shift trace-metal lability in connected riparian zones is therefore important for environmental risk assessment and for understanding how hydrologic connectivity governs watershed-scale ERW impacts.

Against this backdrop, we evaluated trace metal behavior during a watershed-scale ERW field trial in a working Vermont dairy agroecosystem. Finely crushed, Fe–Al-rich basalt (20 t ha^{-1}) was surface-applied to paired hayfield and pasture plots with untreated controls, and we monitored a riparian corridor downslope of the treated fields, including a Central Riparian Corridor and an adjacent Wooded Riparian Study Area that are hydrologically connected to the fields. We combined operational measures of extractable soil metals with forage biomass and

tissue chemistry to evaluate in-field exposure pathways (soil availability and plant uptake), using plant tissues as an integrative check against agronomic and livestock-health guidance values. Given the sensitivity of Ca:Al and pH–extractability relationships to shifts in base-cation status and exchangeable Al, we then used riparian soil chemistry, interpreted in the context of these relationships observed in field plots, to investigate whether laterally transported weathering products reduce or increase metal lability beyond the amendment footprint.

Building on this design, we addressed three related questions. First, do basalt applications change concentrations of extractable trace metals in hayfield and pasture soils relative to controls, and are any changes consistent with pH-driven controls on lability? Second, do forage plants show altered metal uptake or biomass production after basalt application relative to agronomic expectations for mixed-grass systems? Third, do riparian soils receiving runoff and lateral subsurface flow from treated fields exhibit systematic shifts in extractable metals that track alkalinization and base-cation enrichment (including Ca:Al)? By linking soil, plant, and riparian observations within a single hydrologically connected deployment, this study constrains the conditions under which basalt-based ERW can be implemented for CDR without elevating risks of trace metals and investigates how metal lability in riparian soils responds to watershed-scale transport of weathering products.

Materials and methods

Site design

This study was conducted in Watershed 2 (W2) of the Sleepers River Research Watershed (44.47° N, 72.60° W) in northern Vermont (Fig. 1). The watershed has a humid temperate climate. Surficial materials consist of glacial till derived from mica schist and quartzite, and land

use is divided between agriculture and forest (Newell, 1970; Shanley et al., 2015). According to USDA soil maps, the topsoil at the experimental sites is mapped as Cabot loam (fine-loamy, mixed, active, frigid Typic Haplorthod) and is moderately well-drained with slightly acidic to near-neutral surface horizons (approximately pH 5.5–7.0). Agricultural liming has not been recorded in the study area over the past two decades.

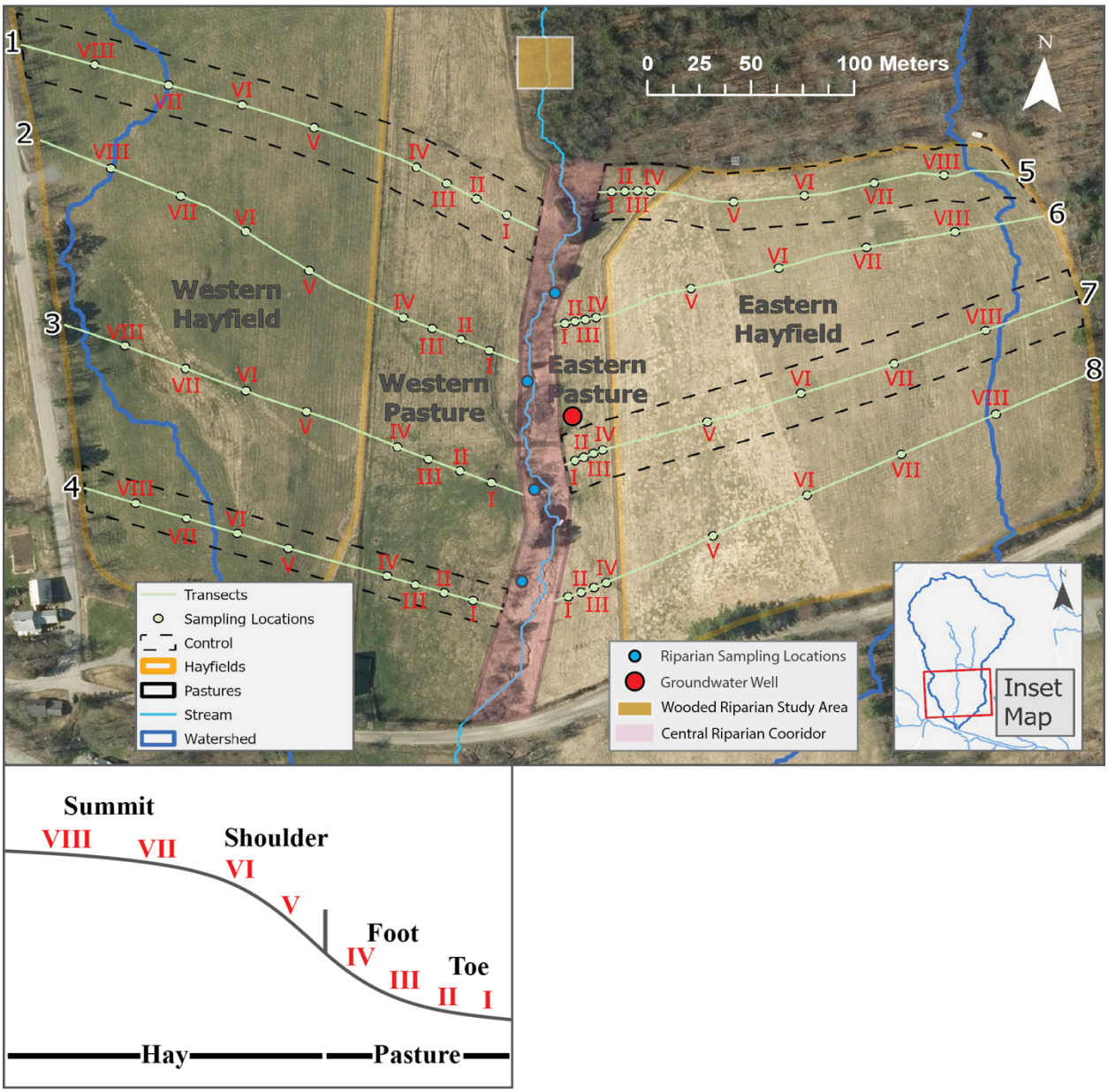

Fig. 1. Map of the 59 ha, first-order agricultural watershed in northern Vermont (Watershed 2 [W2]) showing the experimental layout and riparian sampling context. Four enclosed fields are delineated by land use, including western and eastern pastures and western and eastern hayfields, separated by the Central Riparian Corridor. Basalt was applied throughout the pasture and hayfield areas except for exclusion zones delineated by dashed lines. Upland sampling transects run parallel to the primary hillslope gradient from the field edges toward the riparian zone and are shown for reference. The Central Riparian Corridor (shaded in pink) includes riparian soil sampling plots (blue circles) used for corridor-scale inventory calculations and the shallow groundwater monitoring well (red circle). The Wooded Riparian Study Area, shown as a gold polygon outlined in white, is located north of the Central Riparian Corridor and includes a georeferenced cross-stream soil sampling grid spanning the pasture-facing and forest-facing banks. The stream network is shown in blue, and the watershed boundary is shown in dark blue. The inset map situates the experimental layout within W2. The schematic cross-section beneath the aerial map illustrates the hillslope catena from upland fields through the riparian zone to the stream channel.

We established an ERW field trial across four enclosed agricultural fields in W2 (Fig. 1): western and eastern hayfields and western and eastern pastures separated by a fenced Central Riparian Corridor. Eight transects (1–8) were oriented parallel to the hillslope gradient. Four transects received the basalt amendment (solid light-green lines in Fig. 1) and four were positioned in 30-m wide basalt-exclusion zones and served as untreated controls (dashed black lines in Fig. 1). Each transect contained eight fixed sampling plots (I–VIII) spanning the hillslope catena from lower-slope pasture positions to upper-slope hayfield positions (Fig. 1), yielding 64 agricultural plots (32 control, 32 treated). Finely crushed basalt was surface-applied at 20 t ha^{-1} in summer 2023 to all portions of the pasture and hayfields, except the basalt exclusion zones. Agricultural soils were sampled from the 0–15 cm surface horizon, which captures the primary rooting and nutrient-cycling zone in these grass systems and aligns with routine agricultural soil-testing depth in the northeastern United States.

To evaluate if weathering products affected near-stream reactive interfaces, we sampled riparian soils in (i) the Central Riparian Corridor downslope of the treated fields (blue circles, Fig. 1) and (ii) a Wooded Riparian Study Area (gold polygon, Fig. 1). The sampling layout within the Wooded Riparian Study Area comprised four riparian positions (1–4) spanning both

stream banks (Fig. 2): Positions 1–2 on the west bank adjacent to the treated pasture, and Positions 3–4 on the opposite bank adjacent to the wooded reference area. Each position included four sampling locations (n = 4; total n = 16). We also sampled a shallow groundwater well (1.3 m depth; red circle in Fig. 1) within the riparian corridor for dissolved aluminum using established handling and filtration procedures (Sun et al., 2025).

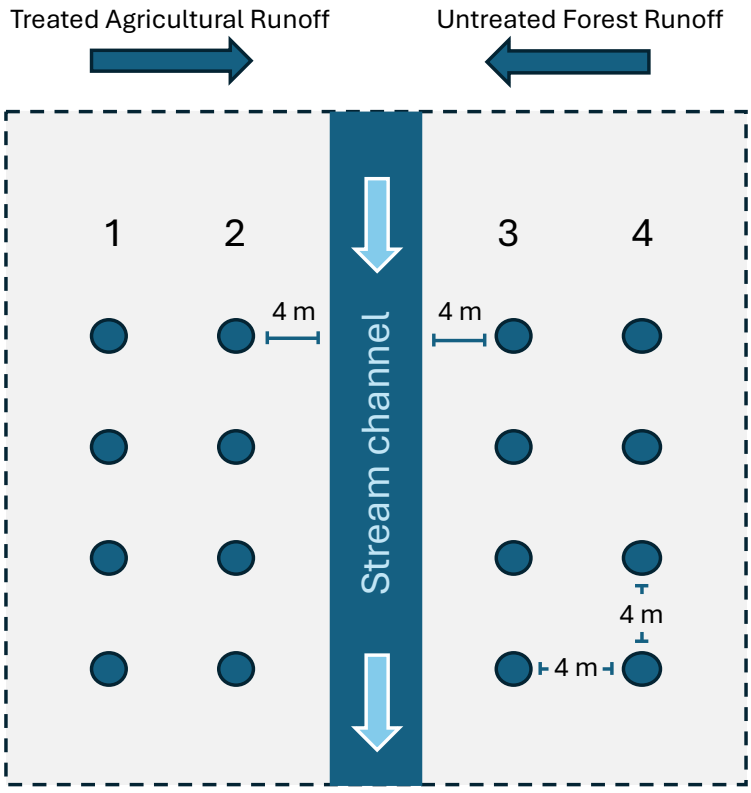

Fig. 2. Cross-stream sampling design in the Wooded Riparian Study Area (north of the Central Riparian Corridor, as delimited by the gold polygon in Figure 1). Positions 1–2 are located on the pasture-facing bank and receive lateral inputs from treated agricultural runoff, whereas positions 3–4 are on the forest-facing bank receiving untreated runoff. Positions 2 and 3 are adjacent to the stream channel. Schematic not to scale. Each riparian position included four replicate sampling locations (n = 4 per position; total n = 16), spaced 4 m apart perpendicular to the primary hillslope gradient; positions themselves were separated by 4 m along that gradient.

Feedstock description

We applied crushed Pioneer Valley basalt sourced from Rock Dust Local at a rate of 20 t ha^{-1} to the soil surface. Major-oxide composition was provided by Rock Dust Local and measured via lithium-metaborate fusion followed by ICP-OES analysis (SiO_2 51.62%, Al_2O_3 13.64%, Fe_2O_3(T) 13.16%, CaO 9.15%, MgO 5.77%, Na_2O 2.98%, K_2O 0.87%). Supplier-reported trace-metal concentrations (TD-ICP and INAA, as specified in the certificate of analysis) were Ni 36 ppm, Cr 24 ppm, Cu 67 ppm, Zn 94 ppm, Pb < 5 ppm, Cd < 0.5 ppm, and As 4 ppm. Powder XRD indicated clinopyroxene and plagioclase with minor alteration phases (sericite, chlorite, actinolite) and oxides, and no olivine. This basalt contains magnetite, a ferromagnetic Fe phase that may enable magnetic tracking of Fe transformation during weathering. Specific surface area (Brunauer–Emmett–Teller) was 4.29 m^2 g^{-1} (Lewis et al., 2021). The feedstock was broadly sand-sized but included a substantial fine fraction: 61.4% < 150 µm and 38.5% < 75 µm; linear interpolation yielded a median particle size of D_{50} = 113 µm, providing high reactive surface area while remaining field-spreadable. Together, these measurements describe an Fe–Al-rich, moderately Ca–Mg basalt suitable for ERW and establish the baseline trace-element loading used to interpret field responses.

Sampling and processing

Soil

Composite surface soils (0–15 cm) were collected from all agricultural (hayfield and pasture) sampling plots and analyzed across six sampling campaigns: two before basalt application (fall 2022 and spring 2023) and four after treatment (fall 2023; spring 2024; fall 2024; spring 2025). For statistical analyses, agricultural plots were grouped into four land-use × hillslope categories based on the catena framework (hayfield summit, hayfield shoulder, pasture foot, pasture toe). For the initial baseline (fall 2022), three 5-cm-diameter cores were collected per plot in the

immediate vicinity of the GPS-referenced location and composited. In subsequent campaigns, eight 1.59-cm-diameter cores were collected per plot and combined and homogenized in the field. All plots were sampled within an approximately 1-m-radius footprint centered on the GPS-referenced location. Samples were placed in labeled bags, kept cool in the field, air-dried at room temperature, sieved to 2 mm, hand-picked to remove coarse roots, homogenized, and subsampled for chemical analysis.

The Central Riparian Corridor and the Wooded Riparian Study Area were sampled on different schedules. In the Central Riparian Corridor, soils were collected once pre-treatment (spring 2023) and during four post-treatment campaigns (fall 2023; spring 2024; fall 2024; spring 2025). Samples were collected from four plots (Fig. 1, blue circles), with eight 1.59-cm-diameter cores taken within a 1-m radius of each plot's GPS-referenced location. In spring 2024, four additional plots were sampled in the Central Riparian Corridor to increase spatial coverage; these samples were collected and processed identically but were included only for that campaign. In the Wooded Riparian Study Area, soils were collected only after basalt application (fall 2024 and spring 2025) using the same coring approach, following a georeferenced cross-stream grid composed of four riparian positions (1–4) spanning both stream banks (Fig. 2). Positions were separated by 4 m along the hillslope gradient, and each position included four sampling locations spaced 4 m apart perpendicular to the gradient (total n = 16). All riparian soils were processed using the same procedures as the agricultural soils.

Forage

Forage vegetation was sampled along hayfield and pasture transects during the first harvest of spring 2023 (pre-treatment) and spring 2024 (one year post-treatment). Forage was collected from odd-numbered plots (I and III in pasture; V and VII in hayfield), yielding 32 plots per

campaign (16 control, 16 treated). We focused on the first harvest because it represents peak standing biomass and provides a consistent basis for comparing hayfield and pasture vegetation. Within each plot, forage was clipped at tractor cutting height (10 cm) from three 0.5 × 0.5 m quadrats (one quadrat in 2023); quadrat locations were randomly selected within plots. All forage samples were air-dried to constant mass, weighed to determine biomass, ground to 2 mm with a Wiley mill, homogenized, and stored prior to digestion for metal analysis.

Forage vegetation within the experimental fields was dominated by orchardgrass (*Dactylis glomerata*), established as a planted monocrop around 2000, but now occurring as a mosaic with naturalized cool-season C_3 grasses and legumes. Common co-occurring grasses included tall fescue (*Festuca arundinacea*), reed canary grass (*Phalaris arundinacea*), and Kentucky bluegrass (*Poa pratensis*), while legumes were dominated by red clover (*Trifolium pratense*) and white clover (*Trifolium repens*); voucher specimens are archived at the Yale Herbarium (Yale Herbarium, 2023). Forbs were less abundant and were dominated by broadleaf plantain (*Plantago major*) and dandelion (*Taraxacum officinale*), and overall species diversity generally increasing toward field margins and the riparian corridor. As expected given management and successional dynamics, orchardgrass was more prevalent in hayfields, whereas pasture plots contained a greater mix of naturally recruited grasses and legumes. Accordingly, vegetation was categorized into four functional classes: planted orchardgrass, wild-seeded grasses, legumes, and forbs.

Chemistry

Target elements and rationale

Target trace metals were defined by the standard analytical suites used for agricultural soil and forage monitoring. We evaluated the full University of Maine agricultural soil screening panel

(Ni, Cr, Pb, Al, Mn, Zn, Cu, Cd) to provide an extension-relevant baseline for detecting anomalous trace-metal behavior under ERW. Nickel (Ni) and chromium (Cr) are of particular relevance because they are characteristic of mafic and ultramafic lithologies and are frequently discussed in ERW-related risk assessments.

For plant tissue analyses, the available panel at the Penn State Agricultural Analytical Services Laboratory included Cu, Mn, and Zn, with Ni and Cr available as optional add-ons. We retained Ni for vegetation monitoring because it is an essential plant micronutrient and is more likely than Cr to be taken up into aboveground biomass under elevated availability, making it a more informative tracer of ERW-related metal mobilization in forage (Fageria et al., 2002; Vink & Knops, 2023). Chromium, which is typically present as Cr(III) and binds strongly to soil minerals, was therefore emphasized for soil interpretation but not included in tissue analyses (Bartlett & James, 1979).

Reporting the complete standard soil and tissue panels enables a conservative, screening-based assessment of ERW-related trace-metal responses across soils, forage, and connected riparian zones without over-interpreting any single element or extraction as a mechanistic measure of bioavailability (Cho et al., 2010; Zimdahl & Skogerboe, 1977).

Soil extractions

Extractable soil metals were quantified using the Modified Morgan extractant and analyzed by ICP–OES at the University of Maine Soil Testing Laboratory. Modified Morgan is the standard trace-metal screening method used by agricultural extension programs in the northeastern United States, including the University of Vermont Extension (Grubinger et al., 2011), and provides an operational measure of readily extractable metal pools that is often interpreted as a proxy for plant-available metals when paired with plant tissue data (Davidson, 2013; McBride et al., 2003;

McBride et al., 2009). Quality assurance/quality control included analytical blanks, continuing-calibration verification standards, certified reference soils, and replicate extractions on 10% of samples to assess analytical accuracy and precision. Elements consistently below analytical detection limits were not reported. Soil pH was measured in a 1:1 (v/w) slurry of air-dried soil and deionized water. Throughout this study, reported increases or decreases in soil metals refer specifically to changes in Modified Morgan–extractable pools (readily exchangeable and weakly complexed metals), rather than to changes in total metal inventories.

Plant tissue digestion

Dried, ground forage samples were digested using concentrated HNO_3 (pre-digestion at 60 °C), followed by a 90-min digestion at 90 °C with addition of 30% H_2O_2. Digestates were analyzed by ICP-OES at Penn State's Agricultural Analytical Services Laboratory for trace metals (Ni, Cu, Zn, Mn). The acid-digestion/ICP-OES workflow and QA/QC procedures followed standard practice for multielement plant analysis, including laboratory blanks, check standards, and certified plant reference materials.

Statistics and data handling

All response variables (Modified Morgan–extractable soil metals, forage biomass, and forage tissue metal concentrations) were natural-log transformed prior to modeling to improve normality and homoscedasticity of residuals, consistent with the right-skewed distributions typical of soil and plant metal data. Statistical significance was evaluated at $\alpha = 0.05$; results with $0.05 < p < 0.1$ are described as approaching statistical significance. Results were also interpreted relative to agronomic guidance thresholds to assess practical significance. Analyses were conducted in R (v4.4.1) using the nlme package.

For agricultural soils, we fit separate linear mixed-effects (LME) models for each extractable metal in the University of Maine soil test panel (Ni, Cr, Pb, Al, Mn, Zn, Cu, Cd), and we fit models separately for hayfield and pasture plots to allow land-use-specific variance structure and interpretation. Within each land use, hillslope position was treated as a two-level factor with a designated reference position: hayfield summit (reference) vs. hayfield shoulder, and pasture foot (reference) vs. pasture toe (see Fig. 1). All soil models included a random intercept for plot to account for repeated measurements through time.

The soil LME regression was specified as:

$$Y_{ijt} = \mu + x_{ij}\beta + 1(t = 2)\,\eta_2 + \sum_{t^*=3}^{6} 1\left(t = t^*\right)\left[\eta_{t^*} + z_{it^*}\left(\alpha_{t^*} + x_{ij}\delta_{t^*}\right)\right] + \phi_{ij} + \varepsilon_{ijt}$$

where Y_{ijt} is the ln-transformed extractable metal concentration at plot j (within transect i) during sampling campaign t; μ is the expected value of Y at baseline time $t = 1$ at the reference hillslope position; x_{ij} is a binary indicator for the non-reference hillslope position (shoulder in hayfields; toe in pastures); β represents the baseline hillslope difference (non-reference relative to reference); z_{it^*} is a binary indicator denoting whether the plot is treated at post-application times ($z = 1$ for treated plots at $t^* = 3$–6; $z = 0$ otherwise); η_2 and η_{t^*} are time fixed effects capturing temporal shifts common to all plots; α_{t^*} quantifies the basalt treatment effect at the reference hillslope position at post-application time t^*; δ_{t^*} quantifies the additional treatment effect at the non-reference position relative to the reference at time t^*; ϕ_{ij} is the plot-level random intercept; and ε_{ijt} is the residual error term. Sampling campaigns were indexed as $t = 1$ (fall 2022), $t = 2$ (spring 2023; pre-application), and post-application $t^* = 3$ (fall 2023), 4 (spring 2024), 5 (fall 2024), and 6 (spring 2025).

The primary parameters of interest were α_{t^*} (treatment effect at the reference position) and the linear combination $\alpha_{t^*} + \delta_{t^*}$ (treatment effect at the non-reference position). We used Wald tests to evaluate these position-specific treatment effects at each post-application sampling campaign, and we back-transformed model coefficients to percent differences on the original scale using $(e^c - 1) \times 100$, where c is the estimated coefficient on the ln scale.

For forage biomass and tissue metals, sampling was limited to odd-numbered plots (I, III, V, VII) during the first harvest in spring 2023 (pre-treatment) and spring 2024 (post-treatment). Accordingly, we used a simplified mixed-effects structure with fixed effects of Treatment (basalt vs. control), Time (2023 vs. 2024), and their interaction (Treatment × Time), and a random intercept for plot. Ln-scale coefficients were interpreted via the same back-transformation to percent change.

When soil extractable metal concentrations were below the analytical limit of detection (LOD), values were substituted with one-half the detection limit (LOD/2) prior to ln transformation to retain a consistent modeling framework; this affected 21% of Cr observations and 4% of Pb observations. To evaluate sensitivity to substitution choice, we repeated Cr models using alternative treatments of <LOD values (exclusion of <LOD observations and substitution with LOD/√2); treatment-effect direction, magnitude, and statistical significance were not meaningfully altered.

Results

Soil and forage risk assessment

Hayfield soil extractable metals

Hayfield plots are presented first because their lower background variability provides a more sensitive test for detecting treatment-related changes in extractable metals. Across all sampling campaigns, extractable metal concentrations were low (median [Q1–Q3], mg kg^{-1}): Ni 0.27 [0.16–0.37], Cr 0.03 [0.01–0.04], Pb 0.85 [0.59–1.09], Cd 0.06 [0.05–0.07], Al 58.28 [43.09–76.69], Mn 9.00 [6.79–11.30], Zn 0.60 [0.43–0.74], and Cu 0.15 [0.13–0.19]. All values were well below Vermont 95th-percentile agronomic screening benchmarks for Ni (0.50), Cr (0.15), Pb (2.20), Zn (6.90), Cu (0.75), and Cd (0.10 mg kg^{-1}). These percentiles are derived from extension soil-testing records across Vermont and represent agronomic screening benchmarks used to contextualize routine soil test results, rather than enforceable regulatory limits (Grubinger et al., 2011). Benchmarks were not available for Al or Mn (Table 1a). Linear mixed-effects models showed no consistent evidence of basalt-driven enrichment in any analyte over the monitoring period (32 plots). Treatment coefficients were generally modest (often within ±20%), but a few larger negative excursions occurred (e.g., Cr −38% at the summit in fall 2023), and four isolated treatment coefficients were statistically significant, including a −36% Cr response at the shoulder position in spring 2025 (Table 2a). Overall, effects were small relative to field variability and did not indicate a systematic basalt-driven increase in extractable metals.

Table 1. Soil and vegetation guideline benchmarks used for interpreting field data.

(a) Modified Morgan–extractable metal percentiles for Vermont agricultural soils (Grubinger et al., 2011). Values represent the statewide median and the Vermont 95th- and 99th-percentile agronomic screening benchmarks based on >11,000 soil tests; "–" denotes data not available.

Element	Median (mg kg^{-1})	95% (mg kg^{-1})	99% (mg kg^{-1})	Number of Tests
Ni	0.15	0.50	1.20	12,252
Cr	0.05	0.15	0.20	11,638
Pb	0.35	2.20	18.30	17,183
Al	–	–	–	–
Mn	–	–	–	–
Zn	1.05	6.90	24.30	17,302
Cu	0.20	0.75	1.75	17,209

Cd	0.05	0.10	2.25	11,958

(b) Interpretive nutrient ranges for orchardgrass tissues (Penn State Agricultural Analytical Services Laboratory, n.d.). Concentrations are classified as low, normal, high, or excessive for forage quality; "–" denotes data not available.

Element	Low (mg kg^{-1})	Normal (mg kg^{-1})	High (mg kg^{-1})	Excessive (mg kg^{-1})
Ni	–	–	–	–
Cu	1	3	6	100
Zn	7	20	51	200
Mn	15	50	151	500

Table 2. Linear mixed-effects model results testing the effect of basalt application on hayfield soil and forage metal concentrations. Percent change values are back-transformed model estimates. Bolded values are statistically significant at $p < 0.05$. Complete regression outputs for the soil models are provided in Table S2, and complete regression outputs for the plant models are provided in Table S3. Treatment effects at the hayfield summit are represented by α terms, and treatment effects at the hayfield shoulder are represented by linear combinations $\alpha + \delta$, following the soil model structure described in Methods. For plant biomass and tissue metals, percent change values represent the Treatment × Time interaction term (2024 treated relative to 2024 control, adjusted for 2023 baseline). Times 3, 4, 5, and 6 correspond to fall 2023, spring 2024, fall 2024, and spring 2025, respectively.

(a) Soil extractable metal concentrations.

Parameter	Parameter Definition	Ni (%)	Cr (%)	Pb (%)	Al (%)	Mn (%)	Zn (%)	Cu (%)	Cd (%)
$\alpha 3$	Treatment, summit, Fall 23	-15.4	**-38.2**	-1.3	-0.4	-13.2	-7.3	-7.8	-3.1
$\alpha 4$	Treatment, summit, Spr 24	-1.7	-1.3	3.7	6.4	-17.2	-11.3	-5.5	-4.0
$\alpha 5$	Treatment, summit, Fall 24	-7.3	8.2	-0.1	1.5	**-21.2**	-20.7	7.3	-2.9
$\alpha 6$	Treatment, summit, Spr 25	24.5	-11.7	-6.9	-7.7	3.4	-12.4	-15.6	**-12.9**
$\alpha 3 + \delta 3$	Treatment, shoulder, Fall 23	-27.7	-15.4	-12.8	-11.3	-5.3	-15.5	-10.1	0.8
$\alpha 4 + \delta 4$	Treatment, shoulder, Spr 24	-15.2	6.3	-10.9	-6.4	-2.4	3.1	-0.3	0.0
$\alpha 5 + \delta 5$	Treatment, shoulder, Fall 24	-6.8	0.2	-12.6	-9.2	-9.9	-16.4	10.2	-6.7

α6 + δ6	Treatment, shoulder, Spr 25	27.4	**-35.7**	-10.9	-9.4	14.9	-15.1	-8.6	-3.0

(b) Plant biomass and tissue metal concentrations

Analyte	Percent Change (%Δ)	Model Estimate (ln)	Standard Error (ln)	Statistic	DF	*P*-Value
Mn	-10.1	-0.107	0.174	-0.617	14.0	0.547
Cu	5.8	0.056	0.125	0.450	28.0	0.656
Zn	-4.8	-0.049	0.102	-0.482	14.1	0.637
Ni	-6.1	-0.063	0.265	-0.236	14.0	0.816
Biomass	-30.9	-0.371	0.714	-0.519	28.0	0.608

Hayfield vegetation metals and biomass

Hayfield forage tissue metal concentrations were low, and we detected no treatment effects. Tissue metal concentrations (median [Q1–Q3], mg kg^{-1}) were Mn 40.68 [35.47–51.61], Cu 9.95 [8.97–11.57], Zn 21.41 [19.62–24.02], and Ni 0.65 [0.46–0.84], all within Penn State Extension interpretive ranges and well below levels considered excessive for orchardgrass (Table 1b). Linear mixed-effects models (Table 2b) indicated no significant Treatment × Time interaction for tissue metal concentrations, indicating that basalt application did not alter forage metal uptake one year post-application relative to controls. Treated plots showed small, non-significant changes, with Mn, Zn, and Ni slightly lower (5–10%) and Cu slightly higher (6%) relative to controls (p = 0.55–0.82). Median baseline forage biomass was 65.0 g m^{-2} (interquartile range: 34.8–94.6 g m^{-2}). Basalt application also did not affect peak aboveground biomass at first cutting (p = 0.61). Together, these forage metrics indicate that basalt application did not measurably alter metal uptake or biomass production within the hayfield during the study period.

Pasture soil extractable metals

Pasture soils showed extractable metal concentrations comparable to hayfields but with greater spatial variability and no clear treatment effect. Across sampling campaigns, concentrations

remained low (median [Q1–Q3], mg kg^{-1}): Ni 0.38 [0.28–0.49], Cr 0.06 [0.04–0.07], Pb 1.25 [0.49–2.26], Cd 0.09 [0.07–0.10], Al 75.37 [25.43–153.03], Mn 13.18 [9.65–20.50], Zn 0.40 [0.27–0.58], and Cu 0.19 [0.15–0.25]. Median concentrations were below Vermont 95th-percentile agronomic screening benchmarks for Ni, Cr, Pb, Zn, Cu, and Cd, although Pb and Cd occasionally approached their 95th-percentile agronomic screening benchmarks (Table 1a). Linear mixed-effects models did not indicate consistent basalt-driven increases in any analyte over the monitoring period (32 plots). Treatment coefficients were often within ±20%, but several larger time- and position-specific effects occurred (e.g., Pb up to 72% at the toe slope in spring 2024 and Ni and Al increases at the toe slope in spring 2025); these effects were isolated, showed no coherent directional pattern across campaigns (Table S1a).

Pasture vegetation metals and biomass

Pasture forage tissue metal concentrations were low, and we detected no treatment effects. Tissue metal concentrations (median [Q1–Q3], mg kg^{-1}) were Mn 86.54 [64.34–96.88], Cu 9.96 [8.08–10.98], Zn 21.99 [19.38–23.85], and Ni 1.16 [0.86–1.61], all within Penn State Extension interpretive ranges and below excessive thresholds for orchardgrass (Table 1b). Linear mixed-effects models (Table S1b) indicated no effect of basalt application on tissue metal concentrations; treated plots showed modest, non-significant increases (4–20%) in Mn, Cu, Zn, and Ni relative to controls (p = 0.42–0.79). Median baseline forage biomass was 37.5 g m^{-2} (interquartile range: 16.9–63.3 g m^{-2}). Basalt application also did not affect peak aboveground biomass at first cutting (p = 0.69). Together, these forage metrics indicate that basalt application did not measurably alter metal uptake or biomass production within the pasture during the study period.

pH as availability control

We examined relations between pH and metal extractability across the full agricultural dataset (hayfield + pasture plots across all sampling campaigns; $n = 304$ observations). Natural log–transformed Modified Morgan–extractable metal concentrations declined consistently with increasing soil pH (1:1 H_2O) (Fig. 3), consistent with strong pH control on cationic metal lability (Alloway, 2012). The strongest inverse correlations were for Pb, Al, Ni, and Zn ($r = -0.507$ to -0.423; $p < 0.001$), with Cd also showing a pronounced negative relationship ($r = -0.378$, $p < 0.001$). Cu, Mn, and Cr exhibited weaker but still significant declines with pH ($r = -0.184$ to -0.166; $p < 0.05$). Across all soil samples from agricultural plots, independent of treatment, extractable metal concentrations declined consistently with increasing soil pH (Fig. 3), indicating that the 0.2 pH unit increase observed following basalt application in this system (Zacharias et al., 2025) would be expected to decrease extractable metal concentrations, rather than increase them, in field soils.

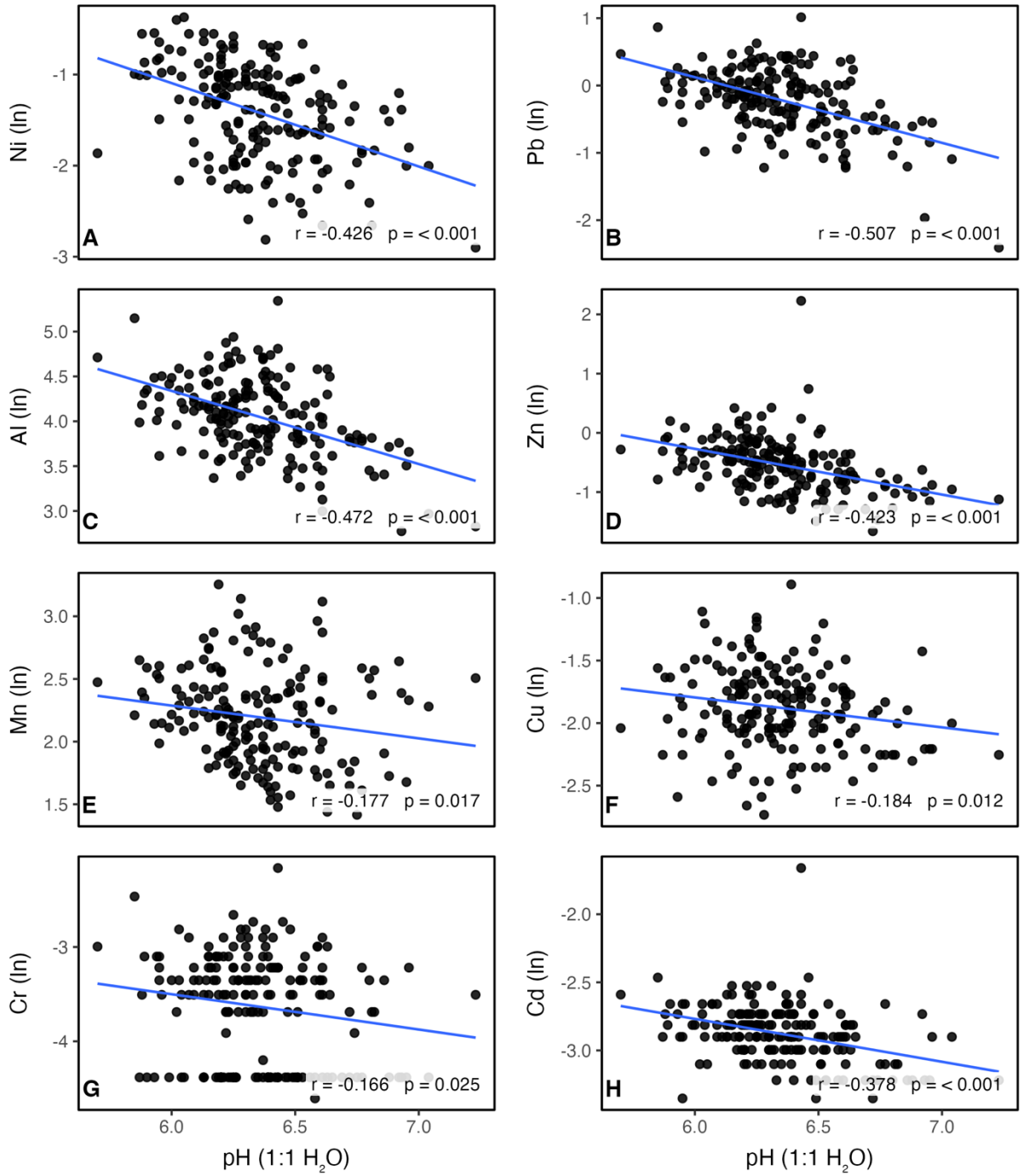

420

421 **Fig. 3.** Relationships between ln-transformed Modified Morgan–extractable metal concentrations and soil
422 pH (1:1 H_2O) across all agricultural plots (hayfield and pasture combined), independent of treatment.
423 Panels show (A) Ni, (B) Pb, (C) Al, (D) Zn, (E) Cd, and (F) Cr. Solid lines represent least-squares linear
424 fits; Pearson correlation coefficients (*r)* and associated *p*-values are shown in each panel. Values below
425 the analytical limit of detection (LOD) were assigned LOD/2 prior to ln transformation and are included
426 in the plots; this substitution results in visible clustering at lower concentrations for analytes with a higher

proportion of values below the LOD (notably Cr). Correlations are interpreted as pattern-level associations reflecting pH-dependent trends in extractable metals.

Riparian zone geochemical controls

We monitored extractable trace metals in the Central Riparian Corridor downslope of the treated pasture (south of the stream's exit from the wooded reach) to assess off-field responses (Fig. 1; sampling plots indicated by blue circles). Sampling included one pre-application baseline (spring 2023) and four post-application campaigns (fall 2023; spring 2024; fall 2024; spring 2025). Within one year after basalt application, Modified Morgan–extractable Ni, Al, and Pb declined sharply and remained low through fall 2024 before showing a modest rebound by spring 2025 (Fig. 4). Reductions were large in magnitude (60–80% decline in campaign means between spring 2023 [pre-application baseline] and spring 2024) and were directionally consistent across all four riparian plots (4/4 sites decreased over this interval). For context, Ni concentrations early in the record fell between the Vermont 95th- and 99th-percentile agronomic screening benchmarks (0.50 and 1.20 mg kg^{-1}, respectively) and declined below the 95th-percentile benchmark after application, while Pb remained well below its 95th-percentile benchmark throughout (2.20 mg kg^{-1}; Table 1a). The largest declines in concentrations in the riparian zones occurred for Ni, Al, and Pb, which also exhibit among the strongest inverse relationships with pH across the full agricultural dataset (Fig. 3). Together, these patterns are most consistent with a pH-driven reduction in metal lability mediated by increased sorption, including inner-sphere surface complexation on mineral and organic surfaces under weathering-derived solute inputs.

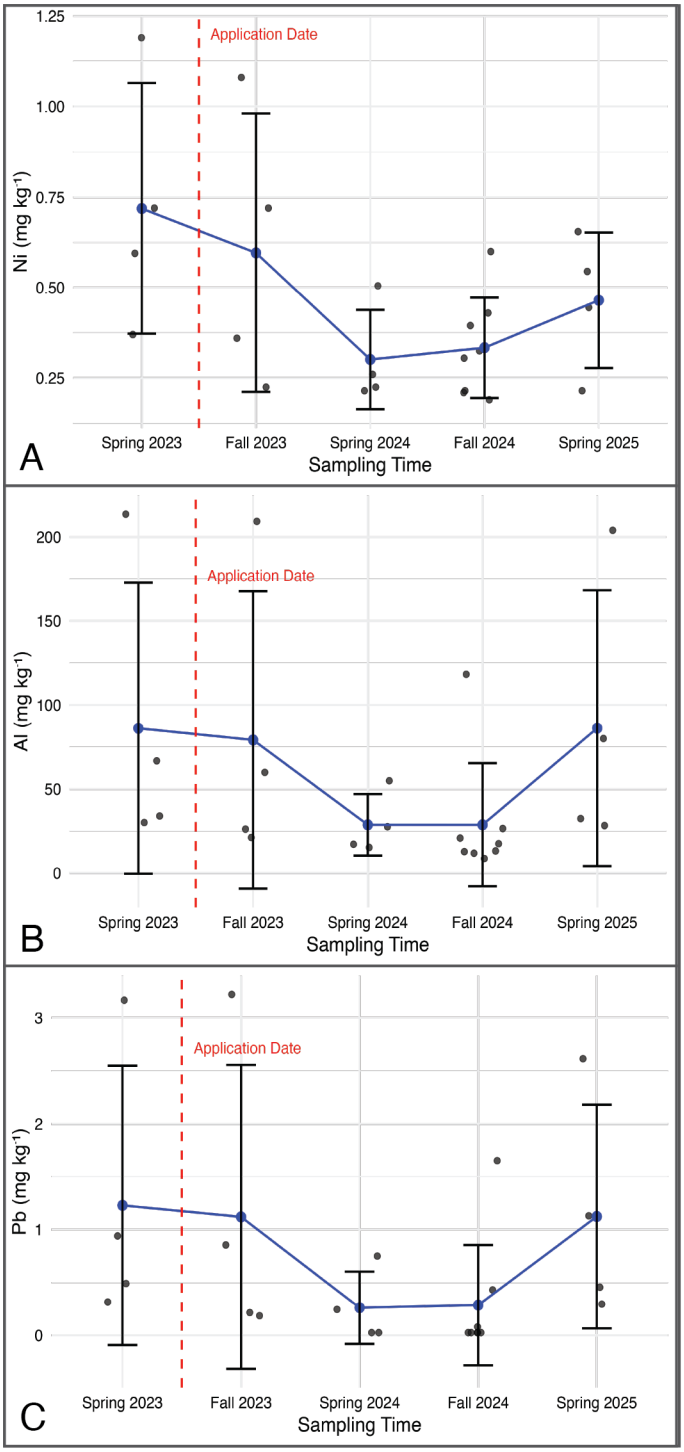

Fig. 4. Temporal trends in extractable metal concentrations in the Central Riparian Corridor following basalt application. Time series of Modified Morgan–extractable Ni (A), Al (B), and Pb (C) from spring 2023 to spring 2025. The red dashed line marks the timing of basalt application (spring 2023). Points show campaign means with error bars representing ± 1 standard deviation; individual site values are shown in grey. All three metals show pronounced post-application declines that persist through fall 2024.

Other soil extractable metals in the Central Riparian Corridor did not exhibit the sustained post-application decline observed for Ni, Al, and Pb. Chromium, Mn, Cu, and Cd remained low and showed modest variability across campaigns, without a consistent directional trend (Figs. S1a–S1b, S1d–S1e). Zinc modestly increased during 2024 but returned toward baseline by spring 2025 (Fig. S1c).

Basalt application was followed by a pronounced rise in the extractable Ca:Al ratio in Central Riparian Corridor soils (Fig. 5). Mean Ca:Al increased from 52 before application (spring 2023) to 225 by spring 2024 and peaked at 292 in fall 2024 before returning to near-baseline values by spring 2025 (mean 51). Ca:Al is widely used as an integrative indicator of exchange-site buffering and aluminum stress in forest and riparian soils, reflecting the balance between base-cation enrichment and exchangeable Al activity. This transient increase in Ca:Al coincided with 60–80% declines in extractable Ni, Al, and Pb between spring 2023 (pre-application baseline) and spring 2024, indicating that these shifts occurred concurrently within the Modified Morgan–extractable pool. Collectively, these patterns are consistent with enhanced base-cation buffering and pH-mediated strengthening of sorptive retention under weathering-

469 derived solute inputs.

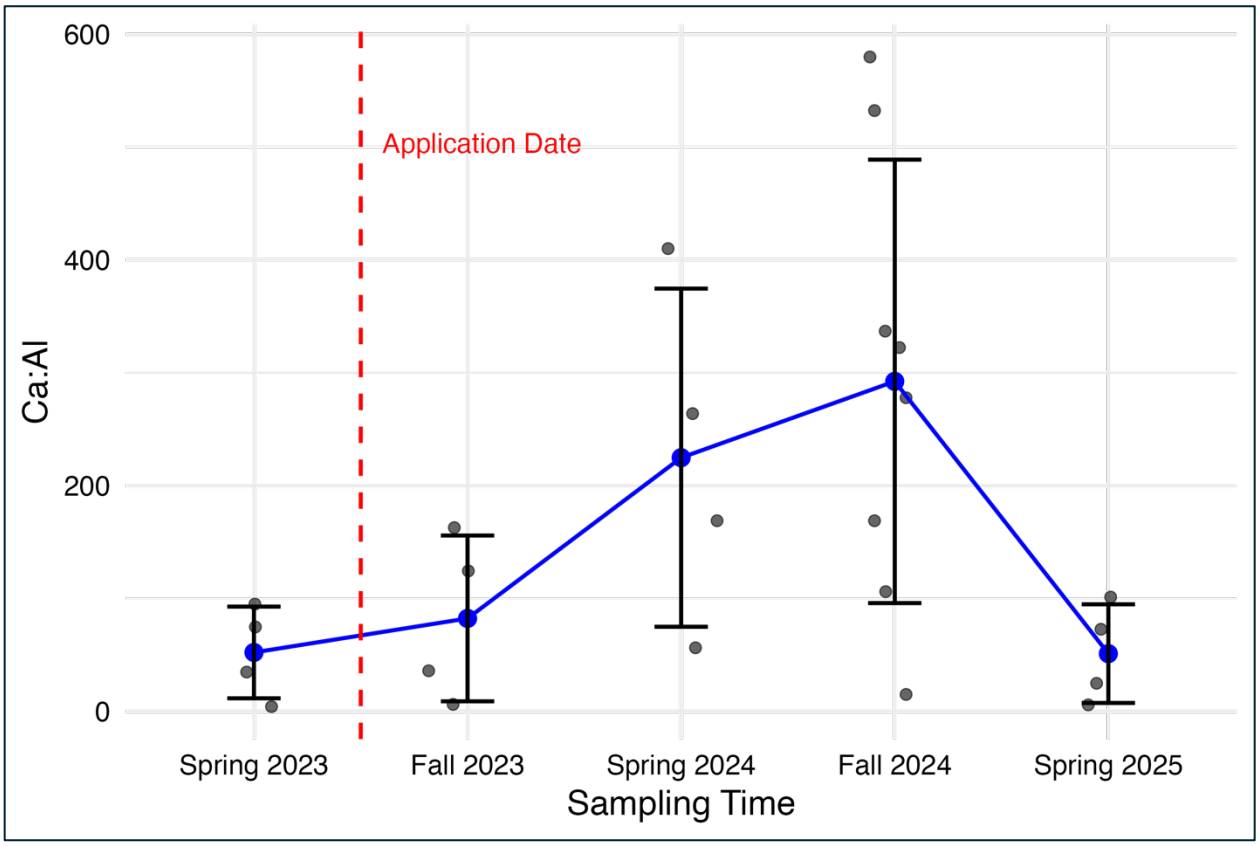

470

471 **Fig. 5.** Temporal trend in the extractable Ca:Al ratio (Modified Morgan Ca divided by Modified Morgan
472 Al) in the Central Riparian Corridor soils from spring 2023 to spring 2025. Following basalt application
473 (red dashed line), mean Ca:Al increased from 52 in spring 2023 to 225 in spring 2024 and peaked at 292
474 in fall 2024 before returning toward baseline by spring 2025 (mean 51). Points show means ± 1 standard
475 deviation with individual site values in grey.

476 To assess whether post-application declines were spatially localized, we examined data
477 from the cross-stream riparian sampling grid in the Wooded Riparian Study Area north of the
478 central corridor (Figs. 1–2). This grid included both stream banks, with two positions on the west
479 bank receiving runoff from the basalt-treated pasture (Position 1 near the pasture edge; Position 2
480 adjacent to the stream) and two positions on the east bank receiving runoff from the untreated
481 forest (Position 3 adjacent to the stream; Position 4 farther upslope). In fall 2024 (>1 year post-
482 application), mean extractable Ni and Al concentrations were approximately two times lower on

the pasture bank than on the forested bank, while Pb exhibited a similar but slightly smaller difference between west and east banks (Fig. 6).

This cross-stream pattern in the Wooded Riparian Study Area persisted through spring 2025, with Ni, Al, and Pb remaining lower on the pasture (treated) bank (Positions 1–2) than at corresponding positions on the forest bank (Positions 3–4) (Fig. 6). In both fall 2024 and spring 2025, the greatest difference in metal concentrations occurred at the stream-adjacent pair (Position 2 on the treated bank versus Position 3 on the forest bank). This spatial signature is consistent with the before–after declines observed in the Central Riparian Corridor. Across both sampling events, concentrations of Ni and Pb on the treated bank remained below the Vermont 95th-percentile agronomic screening benchmark (Table 1a), indicating that the observed shifts represent changes in extractability rather than enrichment from the release of trace metals by dissolution of the basalt feedstock. Other monitored metals (Cr, Mn, Zn, Cu, Cd) showed smaller and/or inconsistent cross-stream structure that varied by position and sampling date (Fig. S2).

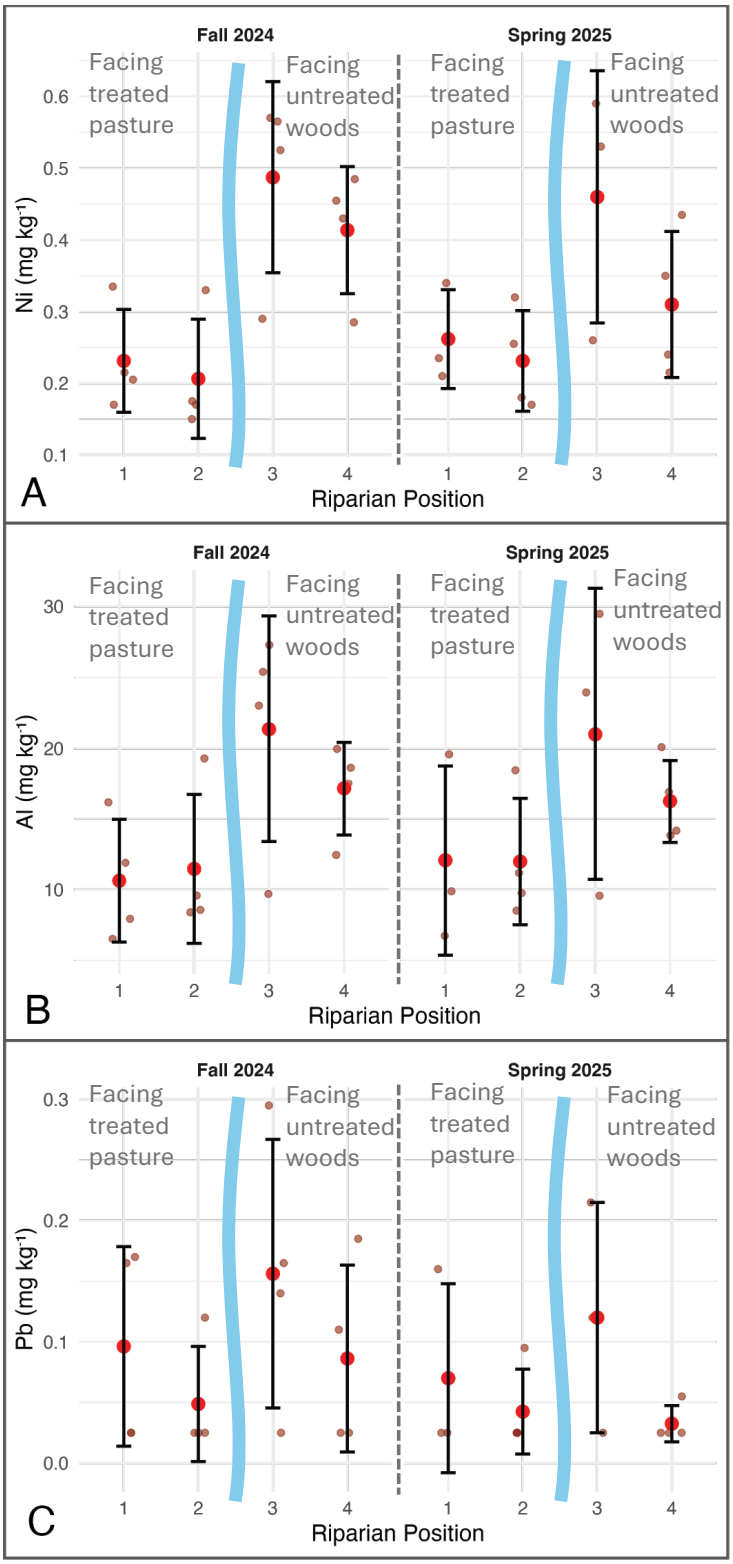
Fall 2024
Spring 2025
Facing treated pasture
Facing untreated woods
Ni (mg kg-1)
0.6
0.5
0.4
0.3
0.2
0.1
1
2
3
4
Riparian Position
A
Al (mg kg-1)
30
20
10
B
Pb (mg kg-1)
0.3
0.2
0.1
0.0
C

Fig. 6. Modified Morgan–extractable Ni (A), Al (B), and Pb (C) across a Wooded Riparian Study Area bordering the basalt-treated pasture, sampled in fall 2024 and spring 2025. Positions 1–2 lie on the treated (pasture-facing) bank (Position 1 nearer the pasture edge; Position 2 nearer the stream), and Positions 3–4 lie on the opposite, untreated forested bank (Position 3 nearer the streambank; Position 4 farther upslope). Metal concentrations were consistently lower on the pasture-facing (treated) bank.

Discussion

Across soils, forage, and riparian zones, the measurements reveal a coherent cross-landscape pattern. In treated agricultural plots, basalt application produced small, statistically non-significant changes in soil extractable metals; modest reductions were more common in hayfields, whereas pasture soils showed more variable effect sizes. These in-field responses were not temporally persistent and were not reflected in forage metal concentrations or biomass. In contrast, riparian soils downslope of treated fields exhibited marked declines in Modified Morgan–extractable Ni, Al, and Pb that coincided with a transient increase in extractable Ca:Al ratios, consistent with enhanced base-cation buffering in riparian soils. Together with the inverse relationships between soil pH and extractable metals across agricultural plots (Fig. 3), these spatially coherent changes suggest that weathering-derived solutes were transported into the riparian corridor along hydrologically connected flow paths, where their delivery of alkalinity and base cations increased exchange-site buffering and reduced metal lability through increased sorptive retention. The contrasting upland versus downslope responses imply that hydrologic connectivity, rather than field-level dissolution alone, governed the observed geochemical outcomes, likely through a combination of saturated-excess overland flow during wet periods (e.g., spring snowmelt), shallow subsurface stormflow, and return flow near the riparian margin (Ledesma et al., 2013; McGlynn et al., 1999; Naiman & DeCamps, 1997), though the relative contributions of these pathways cannot be fully resolved with the available data.

Agricultural risk assessment

Across treated pasture and hayfield plots, we found no evidence of accumulation: trace-metal concentrations in soils and vegetation did not differ between basalt-amended and control treatments, and all values fell within typical Vermont agricultural background ranges (Grubinger et al., 2011). Although some small treatment-related shifts occurred in extractable metals, they were inconsistent in direction and magnitude, remained within background variability, and did not translate into changes in forage metal uptake or biomass. Analytical detection limits for soil and tissue metals were well below these background ranges, indicating that non-detections reflect genuinely low concentrations. The Pioneer Valley basalt used here is an Fe–Al-rich, low-Ni/Cr mafic feedstock (Fe_2O_3(T) = 13.16%, Al_2O_3 = 13.64%, Ni = 36 ppm, Cr = 24 ppm) applied at a modest rate (20 t ha^{-1}), roughly an order of magnitude lower than in some ERW trials (e.g., 200 t ha^{-1}) (Beerling et al., 2024). This Fe–Al–rich composition promotes pH buffering during weathering and increases the potential for sorptive and secondary-phase stabilization of trace metals, consistent with the absence of increased extractable metal concentrations. Extractable Ni remained below the Vermont 95th-percentile agronomic screening benchmark (0.50 mg kg^{-1}) and rarely approached the 99th-percentile benchmark (1.20 mg kg^{-1}). Other metals of agronomic concern (e.g., Cr, Mn, Al) showed no treatment-related increases across sampling campaigns. Likewise, orchardgrass tissue showed no metal accumulation and no biomass reduction; concentrations remained within extension “normal–high” interpretive ranges and were never excessive, even at the first harvest when uptake demand is greatest. These findings are consistent with field-scale basalt ERW studies (Beerling et al., 2024; Bell et al., 2024) and indicate that low trace metal, Fe–Al-rich basalt applied at agronomic rates can

maintain agronomic safety in both soils and forage. Overall, treated–control differences were far below thresholds of agronomic concern and well within natural field heterogeneity.

Riparian attenuation

In contrast to the lack of treatment effects within the amended fields, Modified Morgan–extractable Ni, Pb, and Al declined sharply in the downslope riparian zone (Fig. 4). This pattern is consistent with hydrogeochemical attenuation in which weathering-derived solutes enter organic-rich, fine-textured soils that provide abundant reactive surfaces for metal stabilization (Gu et al., 2017). Although basalt was not applied directly to the riparian corridor, lateral transport of alkalinity and base cations from the treated fields likely contributed to both the transient rise in extractable Ca:Al (Fig. 5) and the concurrent declines in extractable Ni, Pb, and Al, indicating a liming-equivalent influence extending beyond the amendment footprint. These results demonstrate that ERW-induced changes in soil chemistry can propagate downslope along hydrologic flow paths, shifting exchange equilibria and reducing metal lability in receiving soils.

Shallow groundwater adjacent to the riparian zone provides additional context for this response. Dissolved Al exhibited short-term post-application variability in fall 2023, with concentrations remaining within the historical pre-treatment range (Fig. S3a), followed by a marked decline in spring and fall 2024 to values lower than those observed prior to amendment. Over the same interval, groundwater Ca:Al ratios more than doubled beginning in spring 2024 and remained elevated through fall 2024 (Fig. S3b), coincident with the rise in extractable Ca:Al in riparian soils (Fig. 5). This sequence is consistent with a brief period of early exchange adjustment following base-cation inputs, during which small, short-lived increases in dissolved metals may occur, followed by a stronger and more sustained buffering response under elevated

Ca and alkalinity, which promotes metal sequestration. Together with the pH–metal relationships observed across agricultural plots (Fig. 3), these coupled soil and groundwater patterns indicate a dominant net shift toward lower metal availability in the riparian zone.

We note that the riparian component of this study does not constitute a fully paired before–after–control–impact (BACI) design and did not include an independent untreated riparian control corridor monitored through time. While the Central Riparian Corridor was sampled both before and after basalt application, the cross-stream comparison between the treated pasture bank and the opposing forested bank was established only after the intervention. As a result, the spatial contrast alone cannot quantify change relative to a pre-treatment baseline. However, the magnitude and direction of the post-application spatial pattern closely mirror the before–and–after declines observed within the treated riparian corridor, providing convergent evidence that the observed reductions in extractable Ni, Al, and Pb are associated with basalt-derived solute inputs rather than background spatial heterogeneity.

Mechanistic interpretation

Enhanced rock weathering modifies the lability of trace-metals through linked dissolution, acid–base reactions, and changes in sorption (including surface complexation) and secondary-mineral processes. Comminution and early dissolution can release structurally bound metals, producing pulses of dissolved polyvalent metals (e.g., Ni and Cr) as observed for ultramafic feedstocks (te Pas et al., 2023; Ten Berge et al., 2012; Zhang et al., 2024). At the same time, silicate dissolution supplies Ca^{2+}, Mg^{2+}, and alkalinity, raising pH and increasing the negative charge on mineral and organic surfaces, thereby strengthening surface complexation of polyvalent metal cations. Rising pH also promotes Al hydrolysis and can, over time, favor precipitation or transformation of Fe–

Al (hydr)oxide phases that provide additional high-affinity sorption and occlusion sites for trace-metals (Alam et al., 2025; Cho et al., 2010; Cornell & Schwertmann, 2003; Nascimento et al., 2025). Although Ca inputs may transiently displace weakly sorbed metals, pH-driven changes in surface charge and speciation generally favor net scavenging via sorption and, potentially, secondary phase development. The balance between mobilization and scavenging depends on feedstock mineralogy, the supply of reactive Fe–Al relative to Ni–Mg inputs, and hydrologic residence time. Although Si:Mg was fixed for the basalt feedstock used here, comparison with other ERW studies suggests that relative position along the Goldich weathering series modulates whether ERW promotes net trace-metal release or scavenging (Fig. 7).

In our experiment, basalt addition increased soil pH by 0.2 units in agricultural soils (Zacharias et al., 2025), and across agricultural plots extractable metal concentrations were inversely related to soil pH independent of treatment (Fig. 3). Consistent with this mechanistic relationship, substantial post-application declines in extractable Ni, Al, and Pb occurred in riparian soils and were consistent with pH-driven scavenging and mineral-transformation processes dominating any transient mobilization in the net extractable signal. With soil aging, these sorption and mineral-transformation pathways progressively shift metals from labile to non-labile pools (Alloway, 2012; Lock & Janssen, 2003) (Fig. 7).

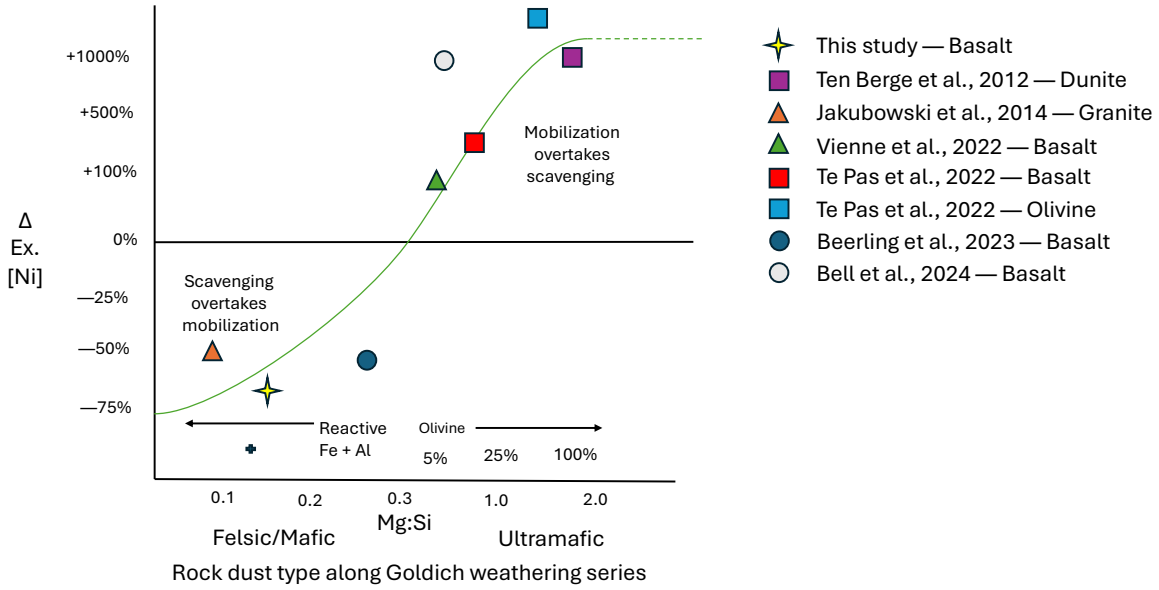

Fig. 7. Conceptual framework illustrating metal dynamics under enhanced rock weathering (ERW). Change in extractable nickel (ΔEx.[Ni]) from ERW studies plotted along Mg:Si ratios from felsic/mafic to ultramafic rock dust compositions, following the Goldich weathering series. Mafic feedstocks with higher reactive Fe + Al tend to promote Ni scavenging (negative ΔEx.[Ni]), whereas ultramafic, olivine-rich materials often exhibit positive ΔEx.[Ni] due to limited secondary oxide formation and scavenging. Star, square, triangle, and circle markers correspond to this study, bench-scale pot and column studies, mesocosm-scale studies, and field-scale studies, respectively.

This mineralogical control on metal mobility is well illustrated in natural systems. Serpentine soils derived from ultramafic parent material contain large total Ni and Cr loads but often maintain low labile fractions: Ni partitions into phyllosilicates and amorphous Fe phases, whereas Cr is retained predominantly as Cr(III) in crystalline oxides and spinels (Nascimento et al., 2025). These patterns highlight both the strength of mineralogical sinks and an asymmetry in metal behavior. Nickel tends to remain more readily extractable, whereas Cr is strongly immobilized unless oxidized to Cr(VI). ERW using Fe–Al-rich mafic rocks such as basalt is therefore expected to favor immobilization pathways, provided pH buffering and secondary-mineral formation shift conditions toward scavenging (Sparks et al., 2022).

Viewed more broadly through a soil-chemical potential lens (Barros et al., 2024; Brantley & White, 2009; Zehe et al., 2019), Fe–Al-rich, low-Ni/Cr basalt ERW drives the aqueous-metal subsystem forward toward a more stable chemical state by shifting metals from labile to sorbed or precipitated pools. Where dissolution releases metals but secondary mineral formation is limited, as in Fe–Al-poor ultramafics, the chemical potential of dissolved metals remains high and lability persists. Cross-study patterns reflect this contrast: Fe–Al-rich mafic rocks typically produce negative ΔEx.[Ni] (net scavenging), whereas olivine-rich mafic and ultramafic materials often show positive ΔEx.[Ni] (net mobilization) (Fig. 7). Short-lived mobilization may precede re-sequestration as secondary phases accumulate (Lewis et al., 2021).

ERW as accelerated pedogenesis

Enhanced rock weathering of low-Ni, Fe–Al-rich mafic feedstocks can accelerate soil-forming reactions that shift trace metals from readily extractable pools to more stable forms. As silicates dissolve, they supply Ca^{2+}, Mg^{2+}, silica, and alkalinity, raising pH and increasing the negative surface charge on minerals and organic matter, thereby strengthening surface complexation of polycationic metals. Over time, higher pH and the addition of reactive Fe–Al may also promote precipitation and aging of Fe–Al (hydr)oxide phases, providing additional high-affinity sorption and occlusion sites (Pohlmann et al., 2016). Fe–Al-rich mafic basalts may therefore favor scavenging, whereas ultramafic feedstocks with limited Fe–Al supply can remain undersaturated and sustain higher metal lability, consistent with serpentine soil analogs (Robinson et al., 1996; Ten Berge et al., 2012). The resulting steady state reflects the balance among dissolution, sorption, and secondary-phase development that sets the labile:non-labile ratio; ERW effectively compresses the time required to reach that state (Vicca et al., 2022; Zhang et al., 2024). Reaction rates are governed by particle size and surface area, moisture regime, and biological inputs

(Bertagni et al., 2024; Deng et al., 2023). Although we did not measure mineralogy directly, magnetic susceptibility and remanence could provide rapid, non-destructive proxies for oxidation of magnetite/titanomagnetite to maghemite–hematite–goethite, and thus help track the development of Fe-oxide scavengers in future ERW monitoring (Jordanova et al., 2024; Mullins, 1977). In our riparian soils, the rise in Ca:Al is consistent with strengthened buffering and reactive binding capacity under basalt-derived solute inputs and coincided with declines in extractable Ni, Al, and Pb.

Implications for ERW deployment

Our field results, together with other ERW studies, indicate that feedstock mineralogy is the primary determinant of agronomic metal safety (Fig. 7). Fe–Al-rich mafic rocks (e.g., basalt) with low Ni and Cr can be applied at agronomic rates without increasing extractable soil metal concentrations or forage metal concentrations. In contrast, ultramafic materials (e.g., olivine, serpentine) contain higher Ni and supply less reactive Fe–Al, making them more prone to Ni mobilization. This conclusion aligns with large field trials reporting negligible metal increases following basalt amendment. In our deployment, the application rate (20 t ha^{-1}) was an order of magnitude lower than in some ERW trials (200 t ha^{-1}) and remained within environmental safety margins (Beerling et al., 2024). Stewardship should nonetheless consider cumulative Ni and Cr loading and track changes in cation-exchange capacity under repeated applications (Haque et al., 2020). Importantly, extrapolating stabilization responses beyond amended areas requires accounting for hydrologic connectivity, which governs the downslope transport of weathering-derived solutes. Practically, these results support feedstock-screening criteria based on total and extractable metal content, Fe–Al buffering capacity, and Ni–Cr composition, and

they suggest that basalt-based ERW can be integrated into existing nutrient-management frameworks (Table 1–2).

Conclusion

Enhanced rock weathering with Fe–Al-rich basalt can be implemented in working agricultural landscapes without increasing trace-metal risks and, where hydrologic connectivity transports weathering products downslope, may reduce extractable metal concentrations in receiving soils. In treated fields, extractable metals and forage tissue concentrations remained within agronomic ranges and yields were unchanged, indicating minimal in-field hazard at agronomic application rates. In contrast, riparian soils downslope of treated plots exhibited marked declines in extractable Ni, Al, and Pb, coincident with a transient rise in Ca:Al ratios, consistent with strengthened base-cation buffering and reduced metal lability. Although specific mineralogical pathways were not directly resolved, the spatial and temporal coherence of soil and groundwater responses supports a pH- and sorption-mediated attenuation mechanism under hydrologic delivery of weathering-derived solutes. These results highlight the importance of feedstock mineralogy and watershed position in governing ERW outcomes and suggest that monitoring frameworks should track soil pH, Ca:Al ratios, and hydrologic connectivity when evaluating trace-metal stewardship.

Acknowledgements

Funding was provided by the Yale Center for Natural Carbon Capture, the Garden Club of America, and the Yale Institute for Biospheric Studies. We thank Rock Dust Local and members of the Saiers lab for their support.

Conflict of interest statement

The authors declare no conflicts of interest.

Data availability statement

The datasets generated and/or analyzed during the current study are available from the corresponding author upon reasonable request.

References

Alam, K. M., Han, J., Kim, B., & Elzinga, E. J. (2025). Nanoscale Observation of Nickel (II) Sequestration by Green Rust Sulfate. *ACS Earth and Space Chemistry*.

Alloway, B. J. (2012). *Heavy metals in soils: trace metals and metalloids in soils and their bioavailability* (Vol. 22). Springer Science & Business Media.

Barros, N., Popovic, M., Molina-Valero, J., Lestido-Cardama, Y., & Pérez-Cruzado, C. (2024). Unravelling the thermodynamic properties of soil ecosystems in mature beech forests. *Scientific Reports*, *14*(1), 16644.

Bartlett, R., & James, B. (1979). *Behavior of chromium in soils: III. Oxidation* (0047-2425).

Beerling, D. J., Epihov, D. Z., Kantola, I. B., Masters, M. D., Reershemius, T., Planavsky, N. J., Reinhard, C. T., Jordan, J. S., Thorne, S. J., & Weber, J. (2024). Enhanced weathering in the US Corn Belt delivers carbon removal with agronomic benefits. *Proceedings of the National Academy of Sciences*, *121*(9), e2319436121.

Beerling, D. J., Kantzas, E. P., Lomas, M. R., Wade, P., Eufrasio, R. M., Renforth, P., Sarkar, B., Andrews, M. G., James, R. H., & Pearce, C. R. (2020). Potential for large-scale CO 2 removal via enhanced rock weathering with croplands. *Nature*, *583*(7815), 242-248.

Beerling, D. J., Reinhard, C. T., James, R. H., Khan, A., Pidgeon, N., & Planavsky, N. J. (2025). Challenges and opportunities in scaling enhanced weathering for carbon dioxide removal. *Nature Reviews Earth & Environment*, 1-15.

Bell, D. S., Epihov, D. Z., Dupla, X., Beerling, D., & Leake, J. R. (2024). Enhanced Rock Weathering in Grassland: Benefits and Risks of Basalt Rock Dust to Soils, Forage Production, and Floristic Diversity in a Slightly Acidic Hay Meadow.

Bertagni, M. B., Calabrese, S., Cipolla, G., Noto, L. V., & Porporato, A. M. (2024). Advancing Enhanced Weathering Modeling in Soils: Systematic Comparison and Validation with Experimental Data. *Authorea Preprints*.

Brantley, S. L., & White, A. F. (2009). Approaches to modeling weathered regolith. *Reviews in mineralogy and geochemistry*, *70*(1), 435-484.

Chiaravalloti, I., Theunissen, N., Zhang, S., Wang, J., Sun, F., Ahmed, A. A., Pihlap, E., Reinhard, C. T., & Planavsky, N. J. (2023). Mitigation of soil nitrous oxide emissions during maize production with basalt amendments. *Frontiers in Climate*, *5*, 1203043.

Cho, Y., Driscoll, C. T., Johnson, C. E., & Siccama, T. G. (2010). Chemical changes in soil and soil solution after calcium silicate addition to a northern hardwood forest. *Biogeochemistry*, *100*(1), 3-20.

Clemens, S., Aarts, M. G., Thomine, S., & Verbruggen, N. (2013). Plant science: the key to preventing slow cadmium poisoning. *Trends in Plant Science*, *18*(2), 92-99.

Cornell, R. M., & Schwertmann, U. (2003). *The iron oxides: structure, properties, reactions, occurrences and uses*. John Wiley & Sons.

Davidson, C. M. (2013). Methods for the determination of heavy metals and metalloids in soils. *Heavy metals in soils: trace metals and metalloids in soils and their bioavailability*, 97-140.

Deng, H., Sonnenthal, E., Arora, B., Breunig, H., Brodie, E., Kleber, M., Spycher, N., & Nico, P. (2023). The environmental controls on efficiency of enhanced rock weathering in soils.

Dupla, X., Claustre, R., Bonvin, E., Graf, I., Le Bayon, R.-C., & Grand, S. (2024). Let the dust settle: Impact of enhanced rock weathering on soil biological, physical, and geochemical fertility. *Science of the total environment*, *954*, 176297.

Fageria, N., Baligar, V., & Clark, R. (2002). Micronutrients in crop production. *Advances in agronomy*, *77*, 185-268.

Flipkens, G., Blust, R., & Town, R. M. (2021). Deriving nickel (Ni (II)) and chromium (Cr (III)) based environmentally safe olivine guidelines for coastal enhanced silicate weathering. *Environmental science & technology*, *55*(18), 12362-12371.

Grubinger, V., Ross, D., & Faulkner, J. (2011). Interpreting the results of soil tests for heavy metals. *University of Vermont*.

Gu, W., Driscoll, C. T., Shao, S., & Johnson, C. E. (2017). Aluminum is more tightly bound in soil after wollastonite treatment to a forest watershed. *Forest Ecology and Management*, *397*, 57-66.

Gupta, S., Vollmer, M., & Krebs, R. (1996). The importance of mobile, mobilisable and pseudo total heavy metal fractions in soil for three-level risk assessment and risk management. *Science of the total environment*, *178*(1-3), 11-20.

Haque, F., Chiang, Y. W., & Santos, R. M. (2020). Risk assessment of Ni, Cr, and Si release from alkaline minerals during enhanced weathering. *Open Agriculture*, *5*(1), 166-175.

Jamieson, H. E., Parsons, M. B., Roches, S. D., Taylor, A. E., Purdy, C. J., Radkova, A. B., Kazamel, B., Turcotte, M. A., Harrison, A. L., & Leybourne, M. I. (2025). The environmental mobility of critical elements in mine waste: rare earth elements, antimony, tungsten, and cobalt. *FACETS*, *10*, 1-11.

Johnson, S. N., Simpson, K. J., & Hartley, S. E. (2025). Could large-scale silicon supplementation of crop-lands mitigate the impacts of climate change? *Plants, People, Planet*.

Jordanova, N., Mokreva, A., Jordanova, D., Tcherkezova, E., & Stoyanova, V. (2024). Mineral magnetic properties of urban forest soils tailored to soil quality indicator. *Catena*, *234*, 107569.

Kelland, M. E., Wade, P. W., Lewis, A. L., Taylor, L. L., Sarkar, B., Andrews, M. G., Lomas, M. R., Cotton, T. A., Kemp, S. J., & James, R. H. (2020). Increased yield and CO2 sequestration potential with the C4 cereal Sorghum bicolor cultivated in basaltic rock dust-amended agricultural soil. *Global Change Biology*, *26*(6), 3658-3676.

Kochian, L. V., Piñeros, M. A., Liu, J., & Magalhaes, J. V. (2015). Plant adaptation to acid soils: the molecular basis for crop aluminum resistance. *Annual review of plant biology*, *66*, 571-598.

Ledesma, J., Grabs, T., Futter, M., Bishop, K. H., Laudon, H., & Köhler, S. (2013). Riparian zone control on base cation concentration in boreal streams. *Biogeosciences*, *10*(6), 3849-3868.

Lewis, A. L., Sarkar, B., Wade, P., Kemp, S. J., Hodson, M. E., Taylor, L. L., Yeong, K. L., Davies, K., Nelson, P. N., & Bird, M. I. (2021). Effects of mineralogy, chemistry and physical properties of basalts on carbon capture potential and plant-nutrient element release via enhanced weathering. *Applied Geochemistry*, *132*, 105023.

Lock, K., & Janssen, C. R. (2003). Influence of aging on metal availability in soils. *Reviews of environmental contamination and toxicology*, 1-21.

Marschner, H. (2011). *Marschner's mineral nutrition of higher plants*. Academic press.

McBride, M., Nibarger, E., Richards, B., & Steenhuis, T. (2003). Trace metal accumulation by red clover grown on sewage sludge-amended soils and correlation to Mehlich 3 and calcium chloride-extractable metals. *Soil Science*, *168*(1), 29-38.

McBride, M., Pitiranggon, M., & Kim, B. (2009). A comparison of tests for extractable copper and zinc in metal-spiked and field-contaminated soil. *Soil Science*, *174*(8), 439-444.

McGlynn, B., McDonnell, J. J., Shanley, J., & Kendall, C. (1999). Riparian zone flowpath dynamics during snowmelt in a small headwater catchment. *Journal of Hydrology*, *222*(1-4), 75-92.

Mullins, C. E. (1977). Magnetic susceptibility of the soil and its significance in soil science–a review. *Journal of soil science*, *28*(2), 223-246.

Nagajyoti, P. C., Lee, K. D., & Sreekanth, T. V. M. (2010). Heavy metals, occurrence and toxicity for plants: a review. *Environmental chemistry letters*, *8*(3), 199-216.

Naiman, R. J., & DeCamps, H. (1997). The ecology of interfaces: Riparian zones. *Annual Review of Ecology and Systematics*, *28*(621–658). https://doi.org/10.1146/annurev.ecolsys.28.1.621

Nascimento, J., Silva, Y., Santos, J., Pedron, F. d. A., Biondi, C., & do Nascimento, C. W. A. (2025). Mineralogical Control and Landscape Influence on Chromium and Nickel Distribution and Bioavailability in Tropical Ultramafic Soils. *Available at SSRN 5199451*.

Newell, W. L. (1970). Factors influencing the grain of the topography along the Willoughby Arch in northeastern Vermont. *Geografiska Annaler: Series A, Physical Geography*, *52*(2), 103-112.

Ni, S., Ju, Y., Hou, Q., Wang, S., Liu, Q., Wu, Y., & Xiao, L. (2009). Enrichment of heavy metal elements and their adsorption on iron oxides during carbonate rock weathering process. *Progress in Natural Science*, *19*(9), 1133-1139.

Olaniran, A. O., Balgobind, A., & Pillay, B. (2013). Bioavailability of heavy metals in soil: impact on microbial biodegradation of organic compounds and possible improvement strategies. *International journal of molecular sciences*, *14*(5), 10197-10228.

Pohlmann, M., Dontsova, K., Root, R., Ruiz, J., Troch, P., & Chorover, J. (2016). Pore water chemistry reveals gradients in mineral transformation across a model basaltic hillslope. *Geochemistry, Geophysics, Geosystems*, *17*(6), 2054-2069.

Power, I. M., Paulo, C., & Rausis, K. (2023). The Mining Industry's Role in Enhanced Weathering and Mineralization for CO2 Removal. *Environmental science & technology*.

Robinson, B. H., Brooks, R. R., Kirkman, J. H., Gregg, P. E., & Gremigni, P. (1996). Plant-available elements in soils and their influence on the vegetation over ultramafic (" serpentine") rocks in New Zealand. *Journal of the Royal Society of New Zealand*, *26*(4), 457-468.

Shanley, J. B., Sebestyen, S. D., McDonnell, J. J., McGlynn, B. L., & Dunne, T. (2015). Water's Way at Sleepers River watershed–revisiting flow generation in a post-glacial landscape, Vermont USA. *Hydrological Processes*, *29*(16), 3447-3459.

Shao, S., Driscoll, C. T., Johnson, C. E., Fahey, T. J., Battles, J. J., & Blum, J. D. (2015). Long-term responses in soil solution and stream-water chemistry at Hubbard Brook after experimental addition of wollastonite. *Environmental Chemistry*, *13*(3), 528-540.

Sparks, D. L., Singh, B., & Siebecker, M. G. (2022). *Environmental soil chemistry*. Elsevier.

Sun, F., Rioux, R., Suhrhoff, T., Tatge, W., Kalderon-Asael, B., Zacharias, Q., Miller-Brown, W., MacDonald, A., Garcia, E., & Shanley, J. (2025). Multiple Lines of Evidence Reveal Rapid, Seasonal Watershed Responses to Enhanced Weathering.

te Pas, E. E., Hagens, M., & Comans, R. N. (2023). Assessment of the enhanced weathering potential of different silicate minerals to improve soil quality and sequester CO2. *Frontiers in Climate*, *4*, 954064.

Ten Berge, H. F., Van der Meer, H. G., Steenhuizen, J. W., Goedhart, P. W., Knops, P., & Verhagen, J. (2012). Olivine weathering in soil, and its effects on growth and nutrient uptake in ryegrass (Lolium perenne L.): a pot experiment.

Vandeginste, V., Lim, C., & Ji, Y. (2024). Exploratory Review on Environmental Aspects of Enhanced Weathering as a Carbon Dioxide Removal Method. *Minerals*, *14*(1), 75.

Vicca, S., Goll, D. S., Hagens, M., Hartmann, J., Janssens, I. A., Neubeck, A., Peñuelas, J., Poblador, S., Rijnders, J., & Sardans, J. (2022). Is the climate change mitigation effect of enhanced silicate weathering governed by biological processes? *Global Change Biology*, *28*(3), 711-726.

Vienne, A., Poblador, S., Portillo-Estrada, M., Hartmann, J., Ijiehon, S., Wade, P., & Vicca, S. (2022). Enhanced weathering using basalt rock powder: carbon sequestration, co-benefits and risks in a mesocosm study with Solanum tuberosum. *Frontiers in Climate*, 72.

Vink, J. P., & Knops, P. (2023). Size-Fractionated Weathering of Olivine, Its CO2-Sequestration Rate, and Ecotoxicological Risk Assessment of Nickel Release. *Minerals*, *13*(2), 235.

Yale Herbarium. (2023). Herbarium catalog of plant species collected by Quinn Zacharias (Catalog Nos. YU.193926–YU.193930). In.

Zacharias, Q., Rioux, R., Sun, F., Tatge, W., Pihlap, E., Nyavor, E., Foster, D., Warren, J. L., Bradford, M. A., & Raymond, P. A. (2025). Spatiotemporal soil fertility responses to an enhanced rock weathering deployment within a temperate, agricultural watershed. *CDRXIV*.

Zehe, E., Loritz, R., Jackisch, C., Westhoff, M., Kleidon, A., Blume, T., Hassler, S. K., & Savenije, H. H. (2019). Energy states of soil water–a thermodynamic perspective on soil water dynamics and storage-controlled streamflow generation in different landscapes. *Hydrology and earth system sciences*, *23*(2), 971-987.

Zhang, B., Kroeger, J., Planavsky, N., & Yao, Y. (2023). Techno-Economic and Life Cycle Assessment of Enhanced Rock Weathering: A Case Study from the Midwestern United States. *Environmental science & technology*, *57*(37), 13828-13837.

Zhang, D., Zeng, Q., Chen, H., Guo, D., Li, G., & Dong, H. (2024). Enhanced Rock Weathering as a Source of Metals to Promote Methanogenesis and Counteract CO2 Sequestration. *Environmental science & technology*, *58*(44), 19679-19689.

Zimdahl, R. L., & Skogerboe, R. K. (1977). Behavior of lead in soil. *Environmental science & technology*, *11*(13), 1202-1207.

Supplemental Information

Table S1. Linear mixed-effects modeling outputs for treatment effects in pasture extractable metal in soil and forage biomass and metal content. Percent change values are back-transformed model estimates. Bolded values are statistically significant at $p < 0.05$. Times 3, 4, 5, and 6 correspond to fall 2023, spring 2024, fall 2024, and spring 2025, respectively.

(a) Treatment response in extractable metal in soil

Parameter	Parameter Definition	Ni (%)	Cr (%)	Pb (%)	Al (%)	Mn (%)	Zn (%)	Cu (%)	Cd (%)
$\alpha 3$	Treatment, foot, Fall 23	14.4	-8.1	22.3	3.6	-6.4	0.7	5.5	0.1
$\alpha 4$	Treatment, foot, Spr 24	-8.0	9.2	26.8	-0.4	-7.4	-9.6	-14.4	-1.3
$\alpha 5$	Treatment, foot, Fall 24	26.6	25.2	-9.2	-5.3	10.2	19.8	27.3	-7.7
$\alpha 6$	Treatment, foot, Spr 25	27.0	2.1	7.1	4.5	3.8	-16.4	12.3	-5.9
$\alpha 3 + \delta 3$	Treatment, toe, Fall 23	**29.4**	-4.9	41.0	13.7	5.7	6.5	22.8	-3.9
$\alpha 4 + \delta 4$	Treatment, toe, Spr 24	-5.3	8.4	**71.8**	**34.6**	-11.9	-20.6	-18.6	-3.0
$\alpha 5 + \delta 5$	Treatment, toe, Fall 24	17.2	16.6	6.8	8.9	10.0	7.7	4.2	-7.3
$\alpha 6 + \delta 6$	Treatment, toe, Spr 25	**43.5**	3.1	11.6	**42.3**	7.4	-23.2	0.7	-4.4

(b) Treatment effects on forage biomass and metal concentrations one year post-application

Analyte	Percent Change (%Δ)	Model Estimate (ln)	Standard Error (ln)	Statistic	DF	P-Value
Mn	20.3	0.185	0.237	0.780	11.7	0.451
Cu	4.3	0.042	0.084	0.506	12.6	0.621
Zn	8.2	0.079	0.094	0.832	10.7	0.423
Ni	6.3	0.061	0.226	0.268	12.8	0.793
Biomass	-22.4	-0.253	0.628	-0.403	13.8	0.693

Table S2. Linear mixed-effects model results for Modified Morgan-extractable trace metals (hayfield).

Models were fit to natural log-transformed Modified Morgan-extractable concentrations. Fixed-effect estimates (β) and standard errors (SE) are reported on the ln scale with 95% confidence intervals (CI). Percent change (%Δ) values are back-transformed as $\%\Delta = 100 \times (\exp(\beta) - 1)$, with CI bounds computed by applying the same transformation to the β-scale CI. Treatment effects at the hayfield summit are represented by α terms (A), and treatment effects at the hayfield shoulder are represented by linear combinations $\alpha + \delta$ (A + d).

(a) Hayfield Ni model results. AIC (ML): 234.83

Term	β	SE	95% CI (β) Lower	95% CI (β) Upper	%Δ	95% CI (%Δ) Lower	95% CI (%Δ) Upper	p-value
Intercept	-1.76	0.08	-1.92	-1.59	—	—	—	<0.001
$\beta 1$	-0.07	0.10	-0.28	0.14	-7.0	-24.5	14.5	0.48
$\eta 2$	0.80	0.09	0.62	0.98	123.4	86.8	167.0	<0.001
$\eta 3$	0.39	0.12	0.15	0.62	47.3	16.5	86.2	0.001
$\eta 4$	0.53	0.12	0.30	0.76	69.9	34.4	114.7	<0.001
$\eta 5$	0.69	0.12	0.45	0.92	99.0	57.4	151.5	<0.001
$\eta 6$	0.70	0.11	0.48	0.91	100.9	62.3	148.7	<0.001
$\alpha 3$	-0.17	0.19	-0.55	0.21	-15.4	-42.0	23.3	0.38
$\alpha 4$	-0.02	0.19	-0.39	0.36	-1.7	-32.6	43.3	0.93
$\alpha 5$	-0.08	0.19	-0.45	0.30	-7.3	-36.4	35.2	0.69
$\alpha 6$	0.22	0.17	-0.11	0.54	24.5	-10.0	72.4	0.188
$\delta 3$	-0.16	0.23	-0.60	0.29	-14.5	-45.3	33.6	0.49
$\delta 4$	-0.15	0.23	-0.59	0.30	-13.7	-44.8	34.9	0.51
$\delta 5$	0.00	0.23	-0.44	0.45	0.5	-35.7	57.0	0.98
$\delta 6$	0.02	0.20	-0.36	0.41	2.3	-30.2	50.0	0.908
$\alpha 3 + \delta 3$	-0.32	0.19	-0.70	0.05	-27.7	-50.2	5.0	0.09
$\alpha 4 + \delta 4$	-0.16	0.19	-0.54	0.21	-15.2	-41.6	23.2	0.39
$\alpha 5 + \delta 5$	-0.07	0.19	-0.44	0.30	-6.8	-35.9	35.4	0.71
$\alpha 6 + \delta 6$	0.24	0.15	-0.06	0.54	27.4	-5.5	71.8	0.112

(b) Hayfield Cr model results. AIC (ML): 277.42

Term	β	SE	95% CI (β) Lower	95% CI (β) Upper	%Δ	95% CI (%Δ) Lower	95% CI (%Δ) Upper	p-value
Intercept	-3.40	0.08	-3.57	-3.24	—	—	—	<0.001
$\beta 1$	0.10	0.09	-0.09	0.29	10.7	-8.2	33.5	0.28
$\eta 2$	-0.41	0.11	-0.62	-0.19	-33.4	-46.2	-17.7	<0.001
$\eta 3$	-0.38	0.14	-0.65	-0.10	-31.4	-47.8	-9.9	0.007
$\eta 4$	0.00	0.14	-0.27	0.28	0.3	-23.7	31.7	0.99
$\eta 5$	-0.66	0.14	-0.93	-0.39	-48.3	-60.6	-32.1	<0.001
$\eta 6$	0.06	0.10	-0.13	0.24	6.0	-12.1	27.7	0.546
$\alpha 3$	-0.48	0.22	-0.91	-0.05	-38.2	-59.7	-5.0	0.03
$\alpha 4$	-0.01	0.22	-0.44	0.42	-1.3	-35.7	51.6	0.95
$\alpha 5$	0.08	0.22	-0.35	0.51	8.2	-29.5	66.2	0.72
$\alpha 6$	-0.12	0.16	-0.43	0.18	-11.7	-34.9	19.7	0.424
$\delta 3$	0.31	0.26	-0.20	0.83	36.7	-18.1	128.2	0.23
$\delta 4$	0.07	0.26	-0.44	0.59	7.7	-35.5	79.8	0.78
$\delta 5$	-0.08	0.26	-0.59	0.44	-7.4	-44.5	54.6	0.77
$\delta 6$	-0.32	0.18	-0.66	0.03	-27.1	-48.6	3.2	0.079
$\alpha 3 + \delta 3$	-0.17	0.22	-0.59	0.26	-15.4	-44.7	29.4	0.44
$\alpha 4 + \delta 4$	0.06	0.22	-0.36	0.49	6.3	-30.5	62.6	0.78
$\alpha 5 + \delta 5$	0.00	0.22	-0.42	0.43	0.2	-34.5	53.3	0.99
$\alpha 6 + \delta 6$	-0.44	0.13	-0.70	-0.19	-35.7	-50.2	-17.0	<0.001

(c) Hayfield Pb model results. AIC (ML): 95.84

Term	β	SE	95% CI (β) Lower	95% CI (β) Upper	%Δ	95% CI (%Δ) Lower	95% CI (%Δ) Upper	*p*-value
Intercept	-0.40	0.11	-0.61	-0.19	—	—	—	<0.001
β1	0.40	0.15	0.10	0.70	49.6	10.8	101.8	0.01
η2	-0.10	0.05	-0.20	0.00	-9.5	-18.2	0.2	0.05
η3	0.06	0.07	-0.09	0.20	5.9	-8.5	22.5	0.44
η4	0.07	0.08	-0.09	0.22	6.7	-8.3	24.2	0.40
η5	-0.02	0.07	-0.15	0.12	-1.5	-13.6	12.2	0.81
η6	0.38	0.08	0.22	0.54	46.6	24.9	71.9	<0.001
α3	-0.01	0.11	-0.24	0.21	-1.3	-21.0	23.3	0.91
α4	0.04	0.13	-0.22	0.29	3.7	-19.4	33.4	0.78
α5	-0.00	0.11	-0.23	0.23	-0.1	-20.4	25.3	0.99
α6	-0.07	0.13	-0.32	0.18	-6.9	-27.6	19.9	0.582
δ3	-0.12	0.13	-0.38	0.13	-11.6	-31.7	14.3	0.34
δ4	-0.15	0.15	-0.44	0.14	-14.1	-35.8	15.0	0.30
δ5	-0.13	0.13	-0.39	0.13	-12.5	-32.6	13.6	0.31
δ6	-0.04	0.15	-0.34	0.25	-4.3	-28.5	28.2	0.769
α3 + δ3	-0.14	0.11	-0.36	0.08	-12.8	-30.0	8.6	0.22
α4 + δ4	-0.12	0.13	-0.36	0.13	-10.9	-30.5	14.1	0.36
α5 + δ5	-0.13	0.11	-0.35	0.09	-12.6	-29.9	8.9	0.23
α6 + δ6	-0.11	0.12	-0.35	0.12	-10.9	-29.4	12.5	0.334

(d) Hayfield Al model results. AIC (ML): 46.48

Term	β	SE	95% CI (β) Lower	95% CI (β) Upper	%Δ	95% CI (%Δ) Lower	95% CI (%Δ) Upper	*p*-value
Intercept	3.96	0.10	3.77	4.15	—	—	—	<0.001
β1	0.30	0.13	0.02	0.57	34.3	2.1	76.7	0.04
η2	-0.16	0.04	-0.24	-0.07	-14.4	-21.6	-6.7	<0.001
η3	-0.04	0.06	-0.16	0.09	-3.8	-15.1	9.1	0.55
η4	0.01	0.07	-0.12	0.14	0.8	-11.6	14.9	0.90
η5	-0.05	0.06	-0.16	0.06	-5.2	-15.1	5.9	0.34
η6	0.46	0.06	0.33	0.59	58.5	39.8	79.8	<0.001
α3	-0.00	0.10	-0.19	0.18	-0.4	-17.6	20.2	0.96
α4	0.06	0.11	-0.15	0.28	6.4	-14.3	32.2	0.57
α5	0.02	0.10	-0.18	0.21	1.5	-16.3	23.1	0.88
α6	-0.08	0.10	-0.28	0.12	-7.7	-24.4	12.7	0.435
δ3	-0.12	0.11	-0.33	0.10	-10.9	-28.3	10.8	0.30
δ4	-0.13	0.13	-0.38	0.12	-12.1	-31.6	13.0	0.31
δ5	-0.11	0.11	-0.33	0.11	-10.5	-28.3	11.7	0.32
δ6	-0.02	0.12	-0.25	0.21	-1.8	-22.0	23.6	0.875
α3 + δ3	-0.12	0.10	-0.31	0.07	-11.3	-26.4	6.9	0.21
α4 + δ4	-0.07	0.11	-0.28	0.15	-6.4	-24.4	15.8	0.54
α5 + δ5	-0.10	0.10	-0.28	0.09	-9.2	-24.6	9.5	0.31
α6 + δ6	-0.10	0.09	-0.28	0.09	-9.4	-24.6	9.0	0.296

(e) Hayfield Mn model results. AIC (ML): -8.43

Term	β	SE	95% CI (β) Lower	95% CI (β) Upper	%Δ	95% CI (%Δ) Lower	95% CI (%Δ) Upper	*p*-value
Intercept	2.43	0.07	2.28	2.58	—	—	—	<0.001
$\beta 1$	-0.24	0.10	-0.44	-0.03	-21.1	-35.9	-2.9	0.03
$\eta 2$	0.10	0.04	0.02	0.18	10.3	2.1	19.3	0.01
$\eta 3$	-0.31	0.06	-0.42	-0.20	-26.7	-34.3	-18.1	<0.001
$\eta 4$	-0.10	0.06	-0.21	0.02	-9.3	-19.0	1.5	0.09
$\eta 5$	-0.15	0.05	-0.25	-0.05	-14.0	-22.5	-4.7	0.004
$\eta 6$	-0.35	0.05	-0.46	-0.25	-29.7	-36.8	-21.8	<0.001
$\alpha 3$	-0.14	0.09	-0.32	0.03	-13.2	-27.1	3.4	0.11
$\alpha 4$	-0.19	0.10	-0.38	0.00	-17.2	-31.4	0.0	0.05
$\alpha 5$	-0.24	0.09	-0.42	-0.06	-21.2	-34.0	-6.0	0.008
$\alpha 6$	0.03	0.09	-0.13	0.20	3.4	-12.6	22.4	0.697
$\delta 3$	0.09	0.10	-0.12	0.29	9.0	-11.0	33.5	0.40
$\delta 4$	0.16	0.11	-0.06	0.38	17.8	-5.4	46.6	0.14
$\delta 5$	0.13	0.10	-0.07	0.34	14.4	-6.8	40.3	0.20
$\delta 6$	0.11	0.10	-0.09	0.30	11.2	-8.5	35.0	0.288
$\alpha 3 + \delta 3$	-0.05	0.09	-0.23	0.12	-5.3	-20.4	12.5	0.53
$\alpha 4 + \delta 4$	-0.02	0.09	-0.21	0.16	-2.4	-19.0	17.5	0.79
$\alpha 5 + \delta 5$	-0.10	0.09	-0.28	0.07	-9.9	-24.2	7.1	0.24
$\alpha 6 + \delta 6$	0.14	0.08	-0.02	0.29	14.9	-1.6	34.3	0.079

(f) Hayfield Zn model results. AIC (ML): 101.63

Term	β	SE	95% CI (β) Lower	95% CI (β) Upper	%Δ	95% CI (%Δ) Lower	95% CI (%Δ) Upper	*p*-value
Intercept	-0.67	0.10	-0.87	-0.47	—	—	—	<0.001
$\beta 1$	0.29	0.14	0.00	0.58	33.7	0.3	78.3	0.05
$\eta 2$	-0.01	0.05	-0.12	0.09	-1.3	-11.1	9.6	0.81
$\eta 3$	0.08	0.08	-0.07	0.23	8.4	-6.6	25.7	0.29
$\eta 4$	-0.00	0.08	-0.16	0.15	-0.4	-14.6	16.1	0.96
$\eta 5$	0.05	0.07	-0.09	0.19	5.0	-8.5	20.5	0.49
$\eta 6$	0.02	0.09	-0.15	0.19	2.0	-14.1	21.1	0.82
$\alpha 3$	-0.08	0.12	-0.31	0.16	-7.3	-26.6	17.1	0.52
$\alpha 4$	-0.12	0.13	-0.38	0.14	-11.3	-31.3	14.5	0.35
$\alpha 5$	-0.23	0.12	-0.47	0.00	-20.7	-37.4	0.4	0.05
$\alpha 6$	-0.13	0.14	-0.40	0.14	-12.4	-33.1	14.8	0.339
$\delta 3$	-0.09	0.14	-0.36	0.18	-8.9	-30.5	19.4	0.50
$\delta 4$	0.15	0.15	-0.15	0.45	16.3	-13.6	56.4	0.32
$\delta 5$	0.05	0.14	-0.22	0.33	5.4	-19.8	38.6	0.70
$\delta 6$	-0.03	0.16	-0.34	0.28	-3.1	-29.2	32.5	0.842
$\alpha 3 + \delta 3$	-0.17	0.12	-0.40	0.06	-15.5	-33.0	6.4	0.15
$\alpha 4 + \delta 4$	0.03	0.13	-0.22	0.28	3.1	-19.9	32.6	0.81
$\alpha 5 + \delta 5$	-0.18	0.12	-0.41	0.05	-16.4	-33.7	5.3	0.13
$\alpha 6 + \delta 6$	-0.16	0.13	-0.41	0.08	-15.1	-33.8	8.9	0.196

(g) Hayfield Cu model results. AIC (ML): 13.81

Term	β	SE	95% CI (β) Lower	95% CI (β) Upper	%Δ	95% CI (%Δ) Lower	95% CI (%Δ) Upper	*p*-value
Intercept	-1.97	0.06	-2.09	-1.86	—	—	—	<0.001
$\beta 1$	0.04	0.08	-0.12	0.19	3.8	-11.3	21.5	0.63
$\eta 2$	-0.07	0.05	-0.16	0.02	-7.1	-15.1	1.6	0.11
$\eta 3$	-0.04	0.06	-0.16	0.08	-4.0	-15.0	8.4	0.51
$\eta 4$	0.34	0.06	0.22	0.47	41.1	24.8	59.5	<0.001
$\eta 5$	0.26	0.06	0.14	0.38	29.1	14.6	45.6	<0.001
$\eta 6$	0.22	0.07	0.09	0.36	25.2	9.5	43.1	0.001
$\alpha 3$	-0.08	0.10	-0.28	0.12	-7.8	-24.4	12.4	0.42
$\alpha 4$	-0.06	0.10	-0.26	0.15	-5.5	-22.8	15.6	0.58
$\alpha 5$	0.07	0.10	-0.13	0.27	7.3	-12.0	30.9	0.49
$\alpha 6$	-0.17	0.11	-0.38	0.04	-15.6	-31.4	3.9	0.112
$\delta 3$	-0.02	0.12	-0.26	0.21	-2.5	-22.6	23.0	0.83
$\delta 4$	0.05	0.12	-0.18	0.29	5.5	-16.7	33.7	0.65
$\delta 5$	0.03	0.12	-0.21	0.26	2.7	-18.6	29.6	0.82
$\delta 6$	0.08	0.12	-0.16	0.32	8.3	-15.0	38.1	0.519
$\alpha 3 + \delta 3$	-0.11	0.10	-0.30	0.09	-10.1	-26.1	9.4	0.29
$\alpha 4 + \delta 4$	-0.00	0.10	-0.20	0.20	-0.3	-18.3	21.7	0.98
$\alpha 5 + \delta 5$	0.10	0.10	-0.10	0.29	10.2	-9.4	34.1	0.33
$\alpha 6 + \delta 6$	-0.09	0.10	-0.28	0.10	-8.6	-24.4	10.6	0.357

(h) Hayfield Cd model results. AIC (ML): -166.22

Term	β	SE	95% CI (β) Lower	95% CI (β) Upper	%Δ	95% CI (%Δ) Lower	95% CI (%Δ) Upper	*p*-value
Intercept	-2.90	0.04	-2.98	-2.81	—	—	—	<0.001
$\beta 1$	0.15	0.06	0.03	0.27	16.2	3.0	31.0	0.02
$\eta 2$	-0.10	0.03	-0.16	-0.05	-9.9	-14.5	-5.1	<0.001
$\eta 3$	-0.10	0.04	-0.17	-0.02	-9.1	-15.6	-2.2	0.01
$\eta 4$	-0.01	0.04	-0.08	0.07	-0.6	-7.8	7.3	0.88
$\eta 5$	-0.08	0.03	-0.15	-0.01	-7.7	-13.7	-1.2	0.02
$\eta 6$	0.16	0.04	0.08	0.24	17.3	8.3	27.1	<0.001
$\alpha 3$	-0.03	0.06	-0.15	0.08	-3.1	-13.6	8.7	0.59
$\alpha 4$	-0.04	0.06	-0.17	0.09	-4.0	-15.4	8.9	0.52
$\alpha 5$	-0.03	0.06	-0.15	0.09	-2.9	-13.6	9.2	0.62
$\alpha 6$	-0.14	0.06	-0.26	-0.01	-12.9	-23.2	-1.3	0.032
$\delta 3$	0.04	0.07	-0.09	0.17	4.0	-9.0	18.9	0.56
$\delta 4$	0.04	0.07	-0.11	0.19	4.2	-10.0	20.7	0.58
$\delta 5$	-0.04	0.07	-0.18	0.10	-3.9	-16.1	10.0	0.56
$\delta 6$	0.11	0.07	-0.04	0.25	11.4	-3.7	28.9	0.149
$\alpha 3 + \delta 3$	0.01	0.06	-0.11	0.12	0.8	-10.1	13.0	0.89
$\alpha 4 + \delta 4$	0.00	0.06	-0.12	0.12	0.0	-11.7	13.3	1.00
$\alpha 5 + \delta 5$	-0.07	0.06	-0.18	0.04	-6.7	-16.7	4.6	0.24
$\alpha 6 + \delta 6$	-0.03	0.06	-0.15	0.08	-3.0	-13.6	8.9	0.604

Table S3. Linear mixed-effects model results for Modified Morgan-extractable trace metals (pasture). Models were fit to natural log-transformed Modified Morgan-extractable

concentrations. Fixed-effect estimates (β) and standard errors (SE) are reported on the ln scale with 95% confidence intervals (CI). Percent change (%Δ) values are back-transformed as %Δ = 100 × (exp(β) − 1), with CI bounds computed by applying the same transformation to the β-scale CI. Treatment effects at the pasture foot-slope position are represented by α terms (A), and treatment effects at the pasture toe-slope position are represented by linear combinations $\alpha + \delta$ (A + d).

(a) Pasture Ni model results. AIC (ML): 106.49

Term	β	SE	95% CI (β) Lower	95% CI (β) Upper	%Δ	95% CI (%Δ) Lower	95% CI (%Δ) Upper	*p*-value
Intercept	-1.64	0.08	-1.79	-1.49	—	—	—	<0.001
$\beta 1$	-0.19	0.08	-0.35	-0.02	-16.9	-29.4	-2.3	0.027
$\eta 2$	1.12	0.08	0.97	1.27	206.6	163.2	257.1	<0.001
$\eta 3$	0.57	0.09	0.38	0.75	76.1	46.2	112.2	<0.001
$\eta 4$	0.88	0.09	0.69	1.06	140.6	99.7	189.8	<0.001
$\eta 5$	0.67	0.09	0.48	0.85	94.7	61.6	134.5	<0.001
$\eta 6$	0.58	0.09	0.39	0.77	78.8	48.4	115.4	<0.001
$\alpha 3$	0.13	0.14	-0.14	0.40	14.4	-12.7	49.7	0.327
$\alpha 4$	-0.08	0.14	-0.35	0.19	-8.0	-29.7	20.5	0.544
$\alpha 5$	0.24	0.14	-0.03	0.51	26.6	-3.3	65.8	0.086
$\alpha 6$	0.24	0.14	-0.04	0.52	27.0	-4.1	68.1	0.095
$\delta 3$	0.12	0.16	-0.20	0.45	13.2	-18.0	56.2	0.448
$\delta 4$	0.03	0.16	-0.29	0.35	2.9	-25.4	42.0	0.862
$\delta 5$	-0.08	0.16	-0.40	0.25	-7.4	-32.9	27.8	0.637
$\delta 6$	0.12	0.17	-0.21	0.45	13.0	-18.9	57.5	0.467
$\alpha 3 + \delta 3$	0.26	0.13	-0.00	0.52	29.4	-0.0	67.6	0.048
$\alpha 4 + \delta 4$	-0.05	0.13	-0.31	0.20	-5.3	-26.9	22.7	0.677
$\alpha 5 + \delta 5$	0.16	0.13	-0.10	0.42	17.2	-9.4	51.8	0.223
$\alpha 6 + \delta 6$	0.36	0.13	0.11	0.62	43.5	11.1	85.4	0.006

(b) Pasture Cr model results. AIC (ML): 309.85

Term	β	SE	95% CI (β) Lower	95% CI (β) Upper	%Δ	95% CI (%Δ) Lower	95% CI (%Δ) Upper	*p*-value
Intercept	-2.83	0.13	-3.08	-2.58	—	—	—	<0.001
$\beta 1$	0.03	0.12	-0.22	0.27	2.6	-19.5	30.9	0.827
$\eta 2$	-0.19	0.14	-0.47	0.09	-17.1	-37.2	9.3	0.182
$\eta 3$	-0.23	0.17	-0.57	0.10	-20.6	-43.2	10.9	0.174
$\eta 4$	0.17	0.17	-0.16	0.50	18.5	-15.2	65.5	0.317
$\eta 5$	-0.69	0.17	-1.03	-0.36	-50.1	-64.2	-30.3	<0.001
$\eta 6$	-0.34	0.17	-0.68	-0.01	-28.9	-49.1	-0.7	0.045
$\alpha 3$	-0.08	0.24	-0.56	0.39	-8.1	-42.7	47.3	0.724
$\alpha 4$	0.09	0.24	-0.38	0.56	9.2	-31.9	75.1	0.712
$\alpha 5$	0.22	0.24	-0.25	0.70	25.2	-21.9	100.8	0.348
$\alpha 6$	0.02	0.25	-0.47	0.51	2.1	-37.6	67.1	0.934
$\delta 3$	0.03	0.29	-0.53	0.60	3.4	-41.3	82.4	0.906
$\delta 4$	-0.01	0.29	-0.57	0.56	-0.7	-43.7	75.0	0.98

Term	β	SE	95% CI (β) Lower	95% CI (β) Upper	%Δ	95% CI (%Δ) Lower	95% CI (%Δ) Upper	*p*-value
$\delta 5$	-0.07	0.29	-0.64	0.50	-6.9	-47.2	64.1	0.803
$\delta 6$	0.01	0.30	-0.57	0.59	1.0	-43.7	81.1	0.974
$\alpha 3 + \delta 3$	-0.05	0.23	-0.50	0.40	-4.9	-39.3	48.9	0.823
$\alpha 4 + \delta 4$	0.08	0.23	-0.37	0.54	8.4	-31.2	70.9	0.725
$\alpha 5 + \delta 5$	0.15	0.23	-0.30	0.61	16.6	-25.9	83.5	0.504
$\alpha 6 + \delta 6$	0.03	0.23	-0.42	0.49	3.1	-34.6	62.4	0.896

(c) Pasture Pb model results. AIC (ML): 406.05

Term	β	SE	95% CI (β) Lower	95% CI (β) Upper	%Δ	95% CI (%Δ) Lower	95% CI (%Δ) Upper	*p*-value
Intercept	0.27	0.33	-0.38	0.92	—	—	—	0.412
$\beta 1$	-0.68	0.45	-1.59	0.23	-49.2	-79.5	26.1	0.139
$\eta 2$	-0.42	0.14	-0.71	-0.14	-34.6	-50.6	-13.4	0.003
$\eta 3$	-0.28	0.18	-0.64	0.07	-24.7	-47.5	7.8	0.12
$\eta 4$	-0.23	0.18	-0.59	0.13	-20.8	-44.7	13.4	0.201
$\eta 5$	-0.05	0.18	-0.41	0.31	-5.0	-33.7	36.0	0.776
$\eta 6$	-0.09	0.18	-0.45	0.27	-8.3	-36.0	31.3	0.633
$\alpha 3$	0.20	0.28	-0.35	0.75	22.3	-29.4	112.1	0.47
$\alpha 4$	0.24	0.28	-0.31	0.79	26.8	-26.9	119.9	0.395
$\alpha 5$	-0.10	0.28	-0.65	0.45	-9.2	-47.6	57.5	0.729
$\alpha 6$	0.07	0.29	-0.50	0.64	7.1	-39.5	89.6	0.813
$\delta 3$	0.14	0.32	-0.50	0.78	15.2	-39.1	117.9	0.661
$\delta 4$	0.30	0.32	-0.33	0.94	35.4	-28.4	156.1	0.348
$\delta 5$	0.16	0.32	-0.47	0.80	17.6	-37.8	122.4	0.615
$\delta 6$	0.04	0.33	-0.61	0.70	4.2	-45.9	100.7	0.901
$\alpha 3 + \delta 3$	0.34	0.27	-0.18	0.87	41.0	-16.8	138.9	0.198
$\alpha 4 + \delta 4$	0.54	0.27	0.01	1.07	71.8	1.4	191.0	0.043
$\alpha 5 + \delta 5$	0.07	0.27	-0.47	0.60	6.8	-37.3	82.0	0.807
$\alpha 6 + \delta 6$	0.11	0.27	-0.42	0.64	11.6	-34.0	88.8	0.683

(d) Pasture Al model results. AIC (ML): 207.89

Term	β	SE	95% CI (β) Lower	95% CI (β) Upper	%Δ	95% CI (%Δ) Lower	95% CI (%Δ) Upper	*p*-value
Intercept	4.39	0.25	3.90	4.87	—	—	—	<0.001
$\beta 1$	-0.58	0.34	-1.27	0.12	-43.8	-71.9	12.7	0.101
$\eta 2$	-0.21	0.08	-0.37	-0.06	-19.3	-30.8	-5.9	0.007
$\eta 3$	-0.11	0.10	-0.31	0.08	-10.8	-26.8	8.6	0.252
$\eta 4$	-0.04	0.10	-0.24	0.15	-4.3	-21.4	16.5	0.656
$\eta 5$	0.06	0.10	-0.14	0.26	6.1	-12.9	29.2	0.552
$\eta 6$	0.10	0.10	-0.09	0.30	11.1	-8.8	35.2	0.294
$\alpha 3$	0.04	0.15	-0.27	0.34	3.6	-23.5	40.3	0.817
$\alpha 4$	-0.00	0.15	-0.31	0.30	-0.4	-26.4	34.8	0.979
$\alpha 5$	-0.05	0.15	-0.36	0.25	-5.3	-30.0	28.2	0.724

Term	β	SE	95% CI (β) Lower	95% CI (β) Upper	%Δ	95% CI (%Δ) Lower	95% CI (%Δ) Upper	*p*-value
$\alpha 6$	0.04	0.16	-0.27	0.36	4.5	-23.7	43.1	0.781
$\delta 3$	0.09	0.18	-0.26	0.44	9.8	-22.6	55.7	0.6
$\delta 4$	0.30	0.18	-0.05	0.65	35.1	-4.7	91.7	0.091
$\delta 5$	0.14	0.18	-0.21	0.49	15.0	-18.9	63.1	0.431
$\delta 6$	0.31	0.18	-0.05	0.67	36.2	-5.0	95.1	0.092
$\alpha 3 + \delta 3$	0.13	0.15	-0.16	0.42	13.7	-14.9	52.0	0.381
$\alpha 4 + \delta 4$	0.30	0.15	0.01	0.59	34.6	0.7	79.8	0.043
$\alpha 5 + \delta 5$	0.09	0.15	-0.21	0.38	8.9	-18.6	45.6	0.562
$\alpha 6 + \delta 6$	0.35	0.15	0.07	0.64	42.3	6.8	89.7	0.016

(e) Pasture Mn model results. AIC (ML): 145.48

Term	β	SE	95% CI (β) Lower	95% CI (β) Upper	%Δ	95% CI (%Δ) Lower	95% CI (%Δ) Upper	*p*-value
Intercept	2.83	0.14	2.56	3.10	—	—	—	<0.001
$\beta 1$	0.12	0.18	-0.25	0.49	12.7	-22.3	63.5	0.515
$\eta 2$	0.10	0.07	-0.05	0.24	10.0	-4.7	26.9	0.191
$\eta 3$	-0.33	0.09	-0.51	-0.14	-27.8	-39.8	-13.4	<0.001
$\eta 4$	-0.25	0.09	-0.43	-0.07	-22.2	-35.1	-6.6	0.007
$\eta 5$	-0.39	0.09	-0.57	-0.21	-32.2	-43.5	-18.6	<0.001
$\eta 6$	-0.28	0.09	-0.46	-0.10	-24.2	-36.8	-9.1	0.003
$\alpha 3$	-0.07	0.14	-0.34	0.21	-6.4	-29.1	23.6	0.64
$\alpha 4$	-0.08	0.14	-0.35	0.20	-7.4	-29.9	22.2	0.583
$\alpha 5$	0.10	0.14	-0.18	0.37	10.2	-16.5	45.5	0.489
$\alpha 6$	0.04	0.15	-0.25	0.33	3.8	-22.2	38.5	0.798
$\delta 3$	0.12	0.16	-0.20	0.44	12.9	-18.2	55.9	0.458
$\delta 4$	-0.05	0.16	-0.37	0.27	-4.9	-31.1	31.3	0.76
$\delta 5$	-0.00	0.16	-0.32	0.32	-0.2	-27.7	37.8	0.99
$\delta 6$	0.03	0.17	-0.30	0.37	3.5	-25.7	44.2	0.838
$\alpha 3 + \delta 3$	0.06	0.13	-0.21	0.32	5.7	-18.8	37.7	0.677
$\alpha 4 + \delta 4$	-0.13	0.13	-0.39	0.14	-11.9	-32.5	14.9	0.345
$\alpha 5 + \delta 5$	0.10	0.13	-0.17	0.36	10.0	-15.6	43.3	0.477
$\alpha 6 + \delta 6$	0.07	0.13	-0.19	0.33	7.4	-17.3	39.7	0.592

(f) Pasture Zn model results. AIC (ML): 203.82

Term	β	SE	95% CI (β) Lower	95% CI (β) Upper	%Δ	95% CI (%Δ) Lower	95% CI (%Δ) Upper	*p*-value
Intercept	-0.73	0.13	-0.99	-0.47	—	—	—	<0.001
$\beta 1$	-0.16	0.17	-0.50	0.19	-14.4	-39.1	20.5	0.361
$\eta 2$	-0.14	0.09	-0.32	0.04	-13.0	-27.2	3.9	0.122
$\eta 3$	-0.09	0.11	-0.32	0.13	-8.8	-27.1	14.0	0.415
$\eta 4$	0.05	0.11	-0.17	0.28	5.4	-15.8	31.8	0.645
$\eta 5$	-0.37	0.11	-0.59	-0.14	-30.6	-44.6	-13.2	0.002
$\eta 6$	-0.18	0.11	-0.41	0.04	-16.6	-33.4	4.3	0.11

Term	β	SE	95% CI (β) Lower	95% CI (β) Upper	%Δ	95% CI (%Δ) Lower	95% CI (%Δ) Upper	*p*-value
$\alpha 3$	0.01	0.17	-0.33	0.35	0.7	-28.2	41.3	0.966
$\alpha 4$	-0.10	0.17	-0.44	0.24	-9.6	-35.6	26.8	0.555
$\alpha 5$	0.18	0.17	-0.16	0.52	19.8	-14.6	68.0	0.294
$\alpha 6$	-0.18	0.18	-0.53	0.17	-16.4	-41.2	18.9	0.317
$\delta 3$	0.06	0.20	-0.34	0.45	5.7	-28.8	57.1	0.781
$\delta 4$	-0.13	0.20	-0.53	0.27	-12.1	-40.8	30.6	0.52
$\delta 5$	-0.11	0.20	-0.50	0.29	-10.1	-39.5	33.5	0.595
$\delta 6$	-0.09	0.21	-0.49	0.32	-8.2	-38.9	37.9	0.678
$\alpha 3 + \delta 3$	0.06	0.16	-0.26	0.39	6.5	-23.0	47.3	0.701
$\alpha 4 + \delta 4$	-0.23	0.16	-0.55	0.09	-20.6	-42.6	9.8	0.159
$\alpha 5 + \delta 5$	0.07	0.16	-0.25	0.40	7.7	-22.2	48.9	0.653
$\alpha 6 + \delta 6$	-0.26	0.16	-0.59	0.06	-23.2	-44.3	5.8	0.107

(g) Pasture Cu model results. AIC (ML): 73.40

Term	β	SE	95% CI (β) Lower	95% CI (β) Upper	%Δ	95% CI (%Δ) Lower	95% CI (%Δ) Upper	*p*-value
Intercept	-1.82	0.08	-1.97	-1.66	—	—	—	<0.001
$\beta 1$	-0.03	0.09	-0.22	0.15	-3.4	-19.4	15.7	0.697
$\eta 2$	-0.02	0.07	-0.15	0.11	-1.8	-14.0	12.2	0.791
$\eta 3$	0.02	0.08	-0.14	0.19	2.2	-13.3	20.5	0.795
$\eta 4$	0.46	0.08	0.30	0.63	58.6	34.5	86.9	<0.001
$\eta 5$	0.41	0.08	0.25	0.58	51.3	28.3	78.3	<0.001
$\eta 6$	0.13	0.08	-0.03	0.30	14.4	-2.9	34.9	0.107
$\alpha 3$	0.05	0.12	-0.19	0.30	5.5	-17.3	34.6	0.663
$\alpha 4$	-0.16	0.12	-0.40	0.09	-14.4	-32.9	9.2	0.209
$\alpha 5$	0.24	0.12	-0.00	0.49	27.3	-0.2	62.4	0.052
$\alpha 6$	0.12	0.13	-0.14	0.37	12.3	-12.8	44.8	0.366
$\delta 3$	0.15	0.15	-0.14	0.44	16.4	-12.8	55.3	0.301
$\delta 4$	-0.05	0.15	-0.34	0.24	-4.9	-28.7	27.0	0.734
$\delta 5$	-0.20	0.15	-0.49	0.09	-18.2	-38.7	9.2	0.171
$\delta 6$	-0.11	0.15	-0.41	0.19	-10.4	-33.4	20.6	0.465
$\alpha 3 + \delta 3$	0.21	0.12	-0.03	0.44	22.8	-2.8	55.1	0.082
$\alpha 4 + \delta 4$	-0.21	0.12	-0.44	0.03	-18.6	-35.5	2.9	0.082
$\alpha 5 + \delta 5$	0.04	0.12	-0.19	0.27	4.2	-17.5	31.6	0.73
$\alpha 6 + \delta 6$	0.01	0.12	-0.23	0.24	0.7	-20.6	27.5	0.957

(h) Pasture Cd model results. AIC (ML): -27.51

Term	β	SE	95% CI (β) Lower	95% CI (β) Upper	%Δ	95% CI (%Δ) Lower	95% CI (%Δ) Upper	*p*-value
Intercept	-2.50	0.09	-2.68	-2.33	—	—	—	<0.001
$\beta 1$	-0.13	0.12	-0.37	0.11	-12.2	-31.1	11.7	0.278
$\eta 2$	0.02	0.04	-0.07	0.10	1.5	-7.0	10.9	0.731
$\eta 3$	-0.01	0.06	-0.12	0.10	-1.0	-11.5	10.8	0.861

Term	β	SE	95% CI (β) Lower	95% CI (β) Upper	%Δ	95% CI (%Δ) Lower	95% CI (%Δ) Upper	*p*-value
$\eta 4$	0.08	0.06	-0.03	0.19	8.4	-3.1	21.2	0.158
$\eta 5$	0.05	0.06	-0.06	0.16	5.4	-5.8	17.9	0.358
$\eta 6$	0.10	0.06	-0.01	0.22	10.9	-0.8	24.1	0.069
$\alpha 3$	0.00	0.09	-0.17	0.17	0.1	-15.6	18.9	0.987
$\alpha 4$	-0.01	0.09	-0.18	0.16	-1.3	-16.9	17.1	0.876
$\alpha 5$	-0.08	0.09	-0.25	0.09	-7.7	-22.2	9.6	0.359
$\alpha 6$	-0.06	0.09	-0.24	0.12	-5.9	-21.2	12.4	0.501
$\delta 3$	-0.04	0.10	-0.24	0.16	-4.0	-21.3	17.1	0.683
$\delta 4$	-0.02	0.10	-0.22	0.18	-1.7	-19.4	19.9	0.863
$\delta 5$	0.00	0.10	-0.19	0.20	0.4	-17.7	22.5	0.968
$\delta 6$	0.02	0.10	-0.19	0.22	1.6	-17.2	24.7	0.876
$\alpha 3 + \delta 3$	-0.04	0.08	-0.20	0.12	-3.9	-18.4	13.3	0.632
$\alpha 4 + \delta 4$	-0.03	0.08	-0.20	0.13	-3.0	-17.7	14.3	0.709
$\alpha 5 + \delta 5$	-0.08	0.08	-0.24	0.09	-7.3	-21.3	9.2	0.362
$\alpha 6 + \delta 6$	-0.04	0.08	-0.21	0.12	-4.4	-18.7	12.6	0.592

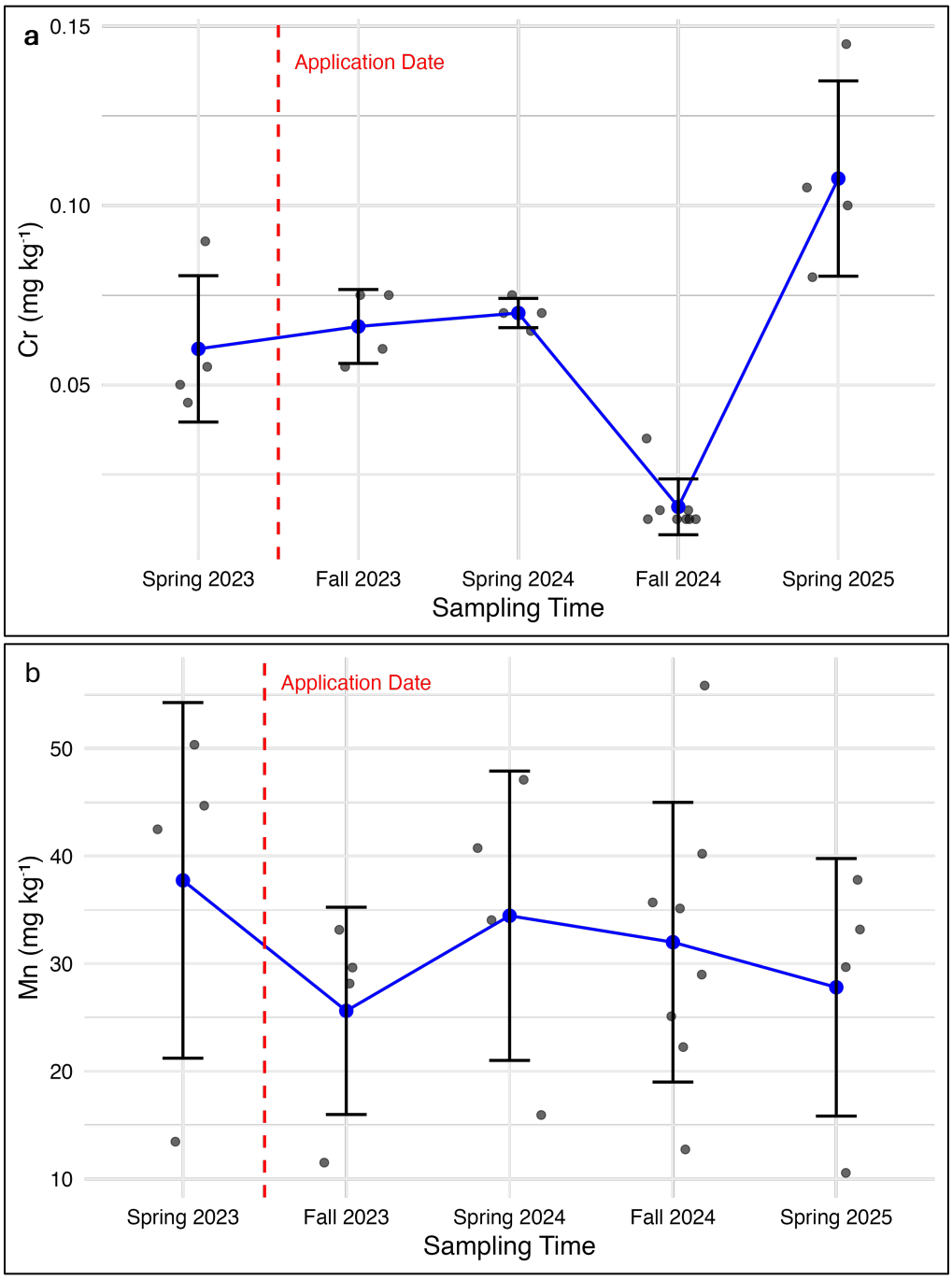
a
0.15
0.10
0.05
Cr (mg kg-1)
Application Date
Spring 2023
Fall 2023
Spring 2024
Fall 2024
Spring 2025
Sampling Time
b
50
40
30
20
10
Mn (mg kg-1)
Application Date
Spring 2023
Fall 2023
Spring 2024
Fall 2024
Spring 2025
Sampling Time

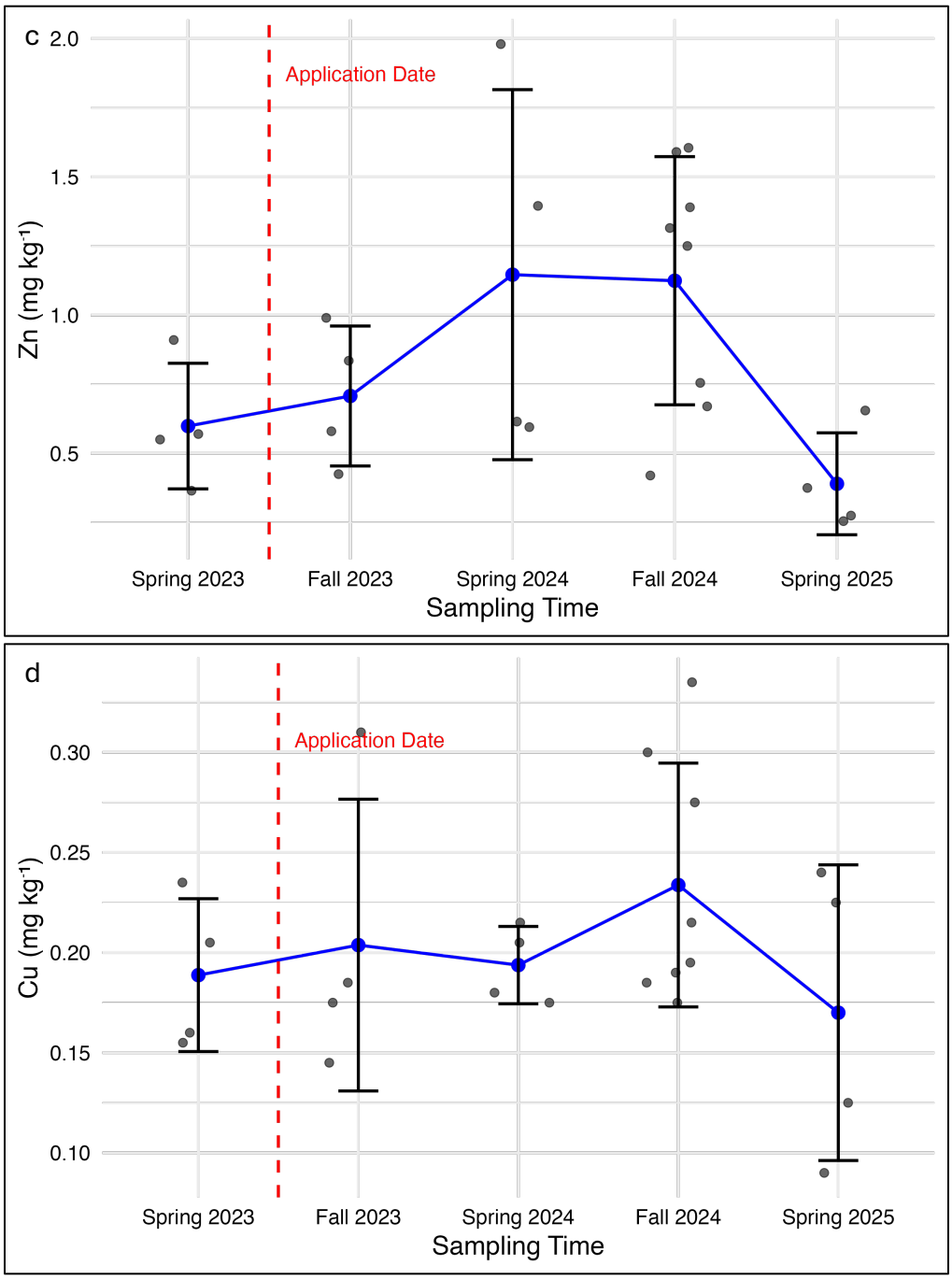
c
2.0
1.5
1.0
0.5
Zn (mg kg-1)
Application Date
Spring 2023
Fall 2023
Spring 2024
Fall 2024
Spring 2025
Sampling Time
d
0.30
0.25
0.20
0.15
0.10
Cu (mg kg-1)
Application Date
Spring 2023
Fall 2023
Spring 2024
Fall 2024
Spring 2025
Sampling Time

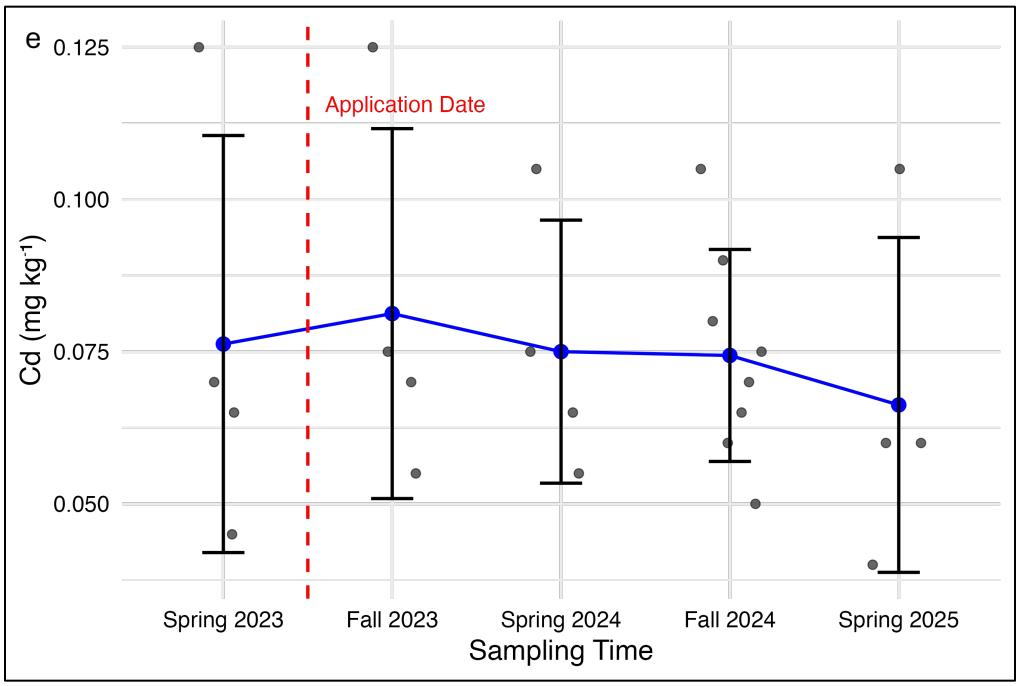

Fig. S1. Time series of soil extractable metal (Cr, Mn, Zn, Cu, Cd) concentrations in the central riparian sampling region. Panels show (a) Cr, (b) Mn, (c) Zn, (d) Cu, (e) Cd. Points represent individual samples; blue symbols and error bars denote mean ± SD. The dashed red line indicates the amendment application date.

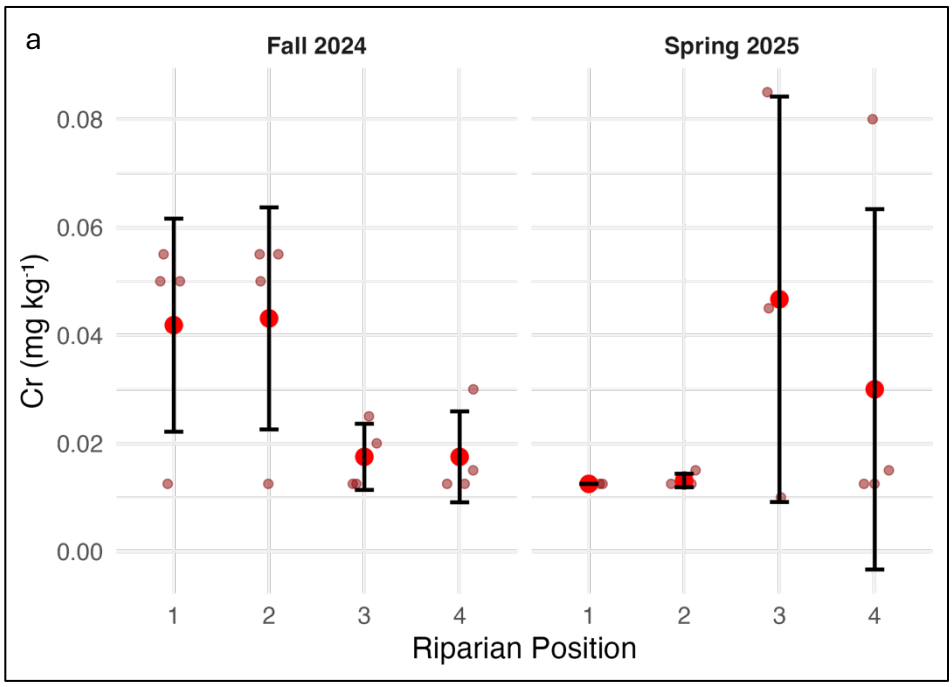

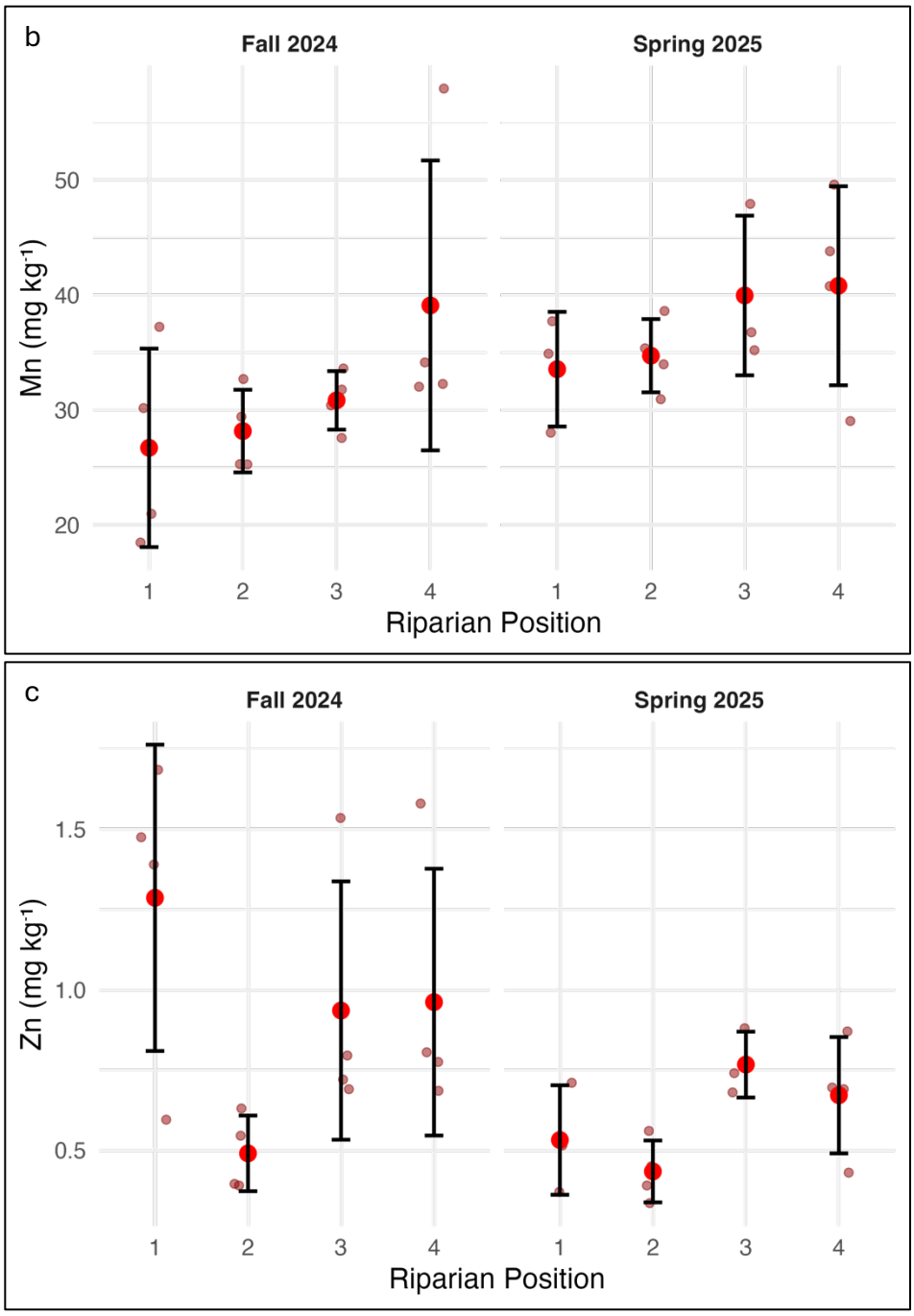
b
Fall 2024
Spring 2025
Mn (mg kg-1)
50
40
30
20
1
2
3
4
Riparian Position
c
Fall 2024
Spring 2025
Zn (mg kg-1)
1.5
1.0
0.5
1
2
3
4
Riparian Position

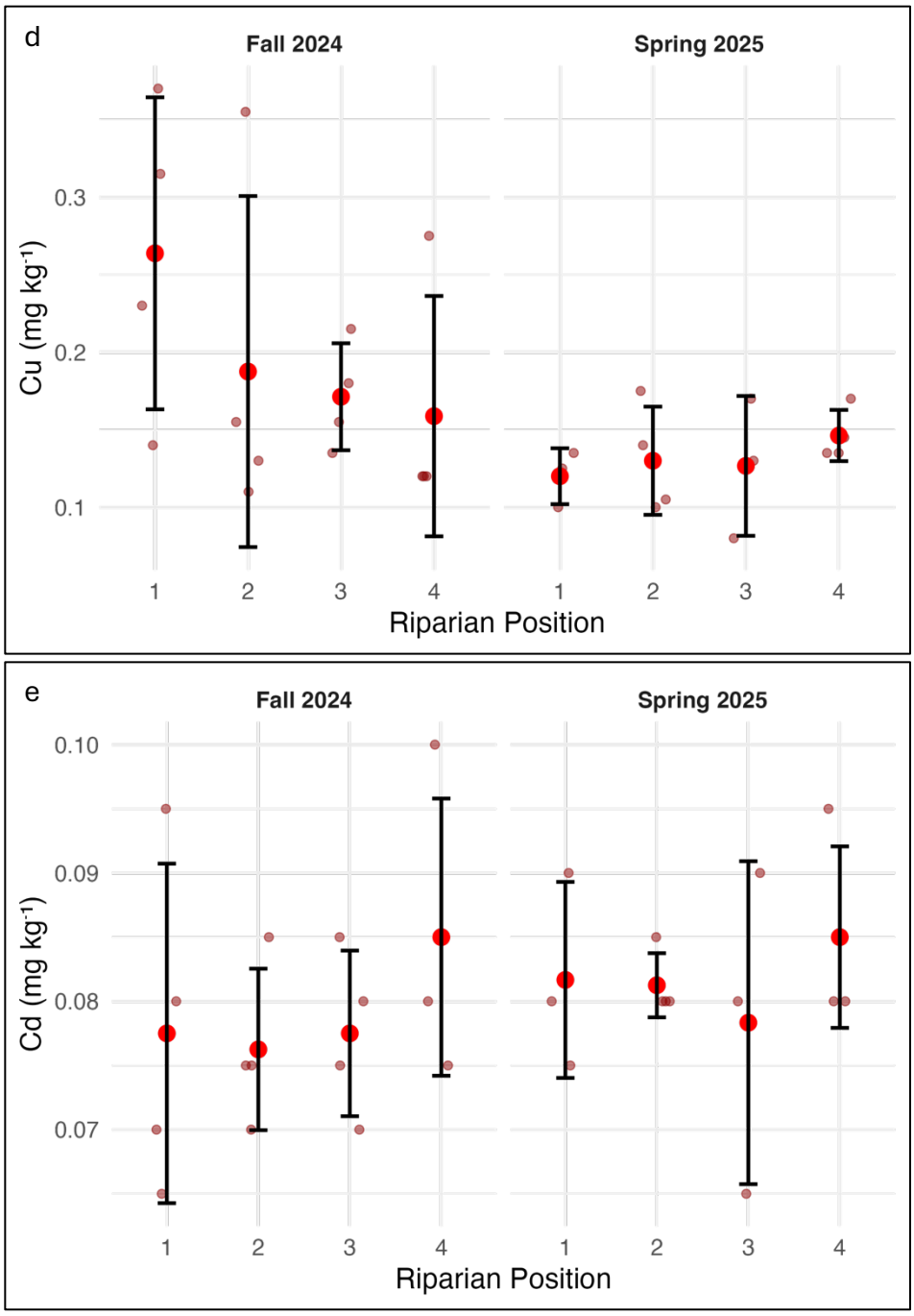

Fig. S2. Extractable metal (Cr, Mn, Zn, Cu, Cd) concentrations across riparian positions (1–4) in the wooded section of the riparian transect during fall 2024 and spring 2025, following basalt application. Panels show (a) Cr, (b) Mn, (c) Zn, (d) Cu, (e) Cd. Positions 1 and 2 are located on the side facing the pasture and received basalt-influenced agricultural runoff, whereas positions 3 and 4 are located on the opposite, untreated forested bank and did not receive basalt influence. The metals shown here represent the remaining analytes not presented in the main text.

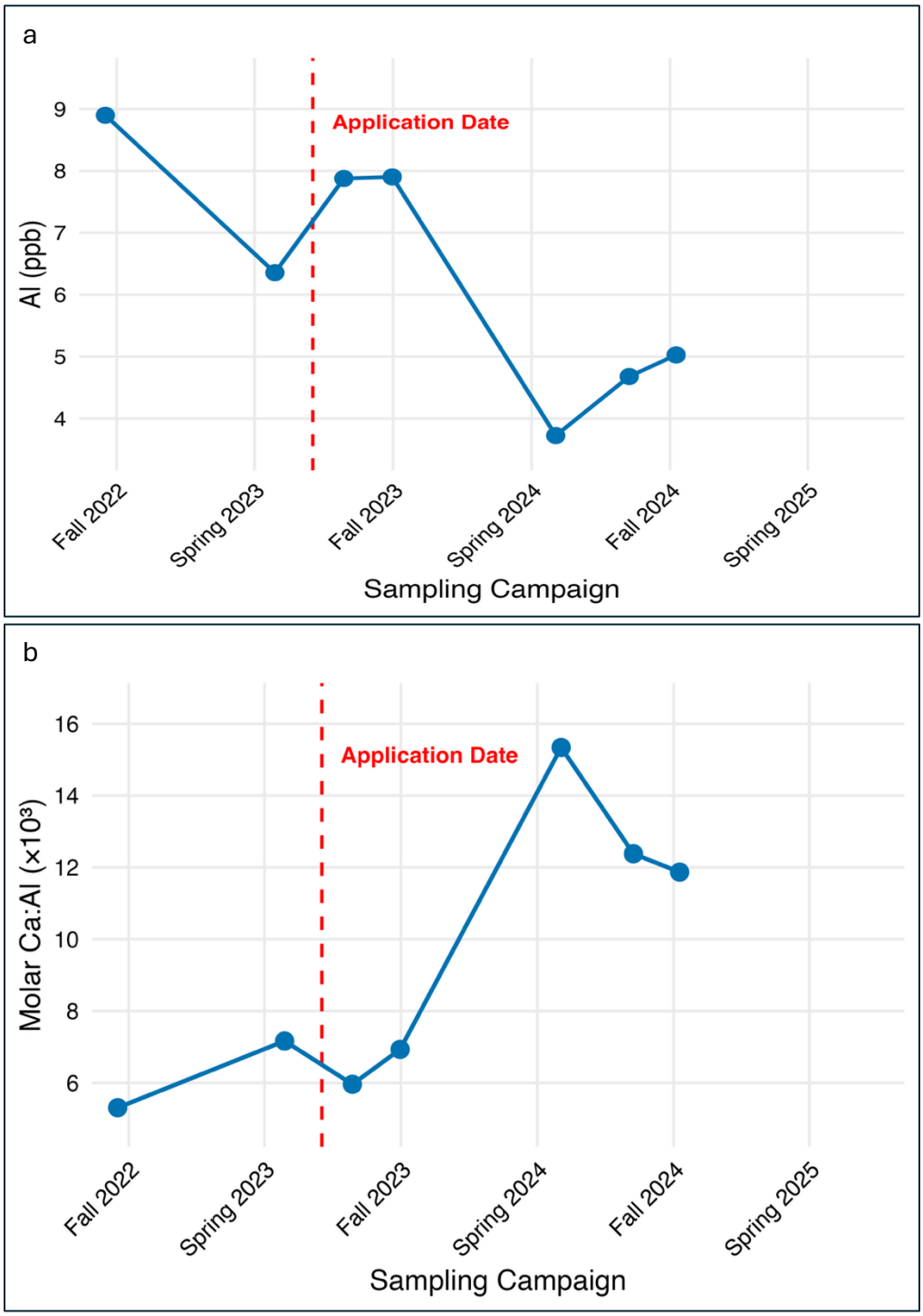

Fig. S3. (a) Dissolved Al and (b) dissolved molar Ca:Al in the shallowest groundwater from Well 10-3 (1.3 m depth) adjacent to the riparian zone. The red dashed line marks basalt application. Dissolved Al exhibited short-term variability in fall 2023, with concentrations remaining within the historical pre-treatment range during the first two post-application campaigns. In subsequent

campaigns, dissolved Al declined to levels lower than those observed prior to application. Groundwater Ca:Al increased beginning in spring 2024 and remained elevated through 2024.